Theses and Dissertations

Spring 2018

Current Induced Depairing and Mixed State Behavior in the Bite/Fete Interfacial Superconductor

Charles Louis Dean II

CURRENT INDUCED DEPAIRING AND MIXED STATE BEHAVIOR IN THE
BITE/FETE INTERFACIAL SUPERCONDUCTOR

by

Charles Louis Dean II

Bachelor of Science
North Georgia College and State University, 2012

Submitted in Partial Fulfillment of the Requirements

For the Degree of Doctor of Philosophy in

Physics

College of Arts and Sciences

University of South Carolina

2018

Accepted by:

Milind Kunchur, Major Professor

Richard Creswick, Committee Member

Timir Datta, Committee Member

Grigory Simin, Committee Member

Cheryl L. Addy, Vice Provost and Dean of the Graduate School

ii

Dedication

I dedicate this thesis to my family, without which I never would have been able to succeed in the ways I have. To my parents, Dan and Nina Dean: Thank you for all of your guidance and support getting me to the point where I believed I could do it. To my lovely and gracious wife, Kason: Thank you for believing in me and assisting me through this journey. No one else could have helped make this a reality quite like you. And to my Son, Charles Ryan Dean: Thank you for giving me a look and plan of what our future may hold together.

Acknowledgements

Abstract

The Bi_2Te_3/FeTe heterostructure intersects several phenomena and key classes of materials in condensed matter physics: topological insulators, superconductivity, magnetism, and the physics of interfaces. While neither the topological insulator (BiTe) nor the iron chalcogenide (FeTe) are themselves superconductors, superconductivity forms in a thin 7nm interfacial layer between the two. The restricted dimensionality and the extraordinarily conductive normal state, possibly sourced by the topologically protected surface states, have led to the observation of novel phenomena such as the Likharev vortex explosion and transitions in behavior resulting from the interplay between current induced depairing and the Berezinski-Kosterlitz-Thouless regime. The measured depairing current density provides information on the magnetic penetration depth and superfluid density, which in turn sheds light on the nature of the normal state that underlies the interfacial superconductivity. We observe a transition in the current-resistance and temperature-resistance curves that quantitatively agrees with the Likharev vortex-explosion phenomenon. In the limit of low temperatures and high current densities, we were able to demonstrate the regime of complete vortex-antivortex dissociation arising from current driven vortex-antivortex pair breaking.

Preface

The driving motivation behind my research comes from a long held love of electromagnetic phenomena. Since a very young age I was interested in what was actually going on inside the various electronic devices in my household. I remember taking apart video game consoles and trying to put them back together. E&M remains to be one of the more intriguing parts of my exploration of the universe.

Superconductivity specifically provides me with countless intricate phenomena to explore. This work is an amalgam of the various projects regarding some of the more novel findings within a new realm of physical systems.

Table of Contents

List of Figures

xi

List of Symbols

T_c Critical temperature

J_d Critical or depairing current density

B_c Generalized critical magnetic field

B_{c1} This is the lower critical field for Type-II superconductors

B_{c2} Upper Critical Field for Type-II superconductors

λ This is the magnetic penetration depth

ξ Superconducting Coherence Length

Ψ Complex Order Parameter Field

n_s Density of superconducting carriers

Δ Superconducting Order Parameter

j_s Supercurrent Density

List of Abbreviations

BCS ....Bardeen-Cooper-Schrieffer

BKT...Berezenski-Kosterlitz-Thouless

BTFT... Bismuth-Telluride/Iron-Telluride

GL .... Ginzburg Landau

ISC ....Interfacial Super Conductor

NTN .... Niobium Titanium Nitride

SC.. Super Conductor

V-aV.. Vortex-antiVortex

CHAPTER 1:
INTRODUCTION TO SUPERCONDUCTIVITY

Superconductivity was first discovered by Dutch physicist Heike Kamerlingh Onnes in 1911. He was looking at transport behavior of elements at extremely low temperatures, using a liquid helium reservoir. While studying mercury, he noticed that the electrical resistance of mercury seemed to disappear at 4.2K. After reheating the material, the effect dissipated. He had stumbled onto something that is one of the most common parameters when categorizing superconductors, namely the critical temperature (TC). He coined the term "superconductivity and won the Nobel Prize of Physics in 1913 for his work. This was so groundbreaking because it had previously been believed by many physicists that all electron movement would halt as a material approached absolute zero.

Walther Meissner and Robert Ochsenfield found that after this critical temperature, superconductors are perfectly diamagnetic. The materials expel all magnetic field during their transition to superconducting state. The experiment was conducted in 1933 using Tin (Sn) and Lead (Pb). Below that critical temperature, they discovered almost all the interior magnetic field was negated. This was an indirect result because they noticed the field at the boundary had increased. This was called the Meissner Effect. This state is linked to the superconducting state and can be broken by applying a significant enough external field. This is another important parameter in the field, known as the "Critical Field" (BC or HC).

1

On theoretical front, Ginzburg-Landau theory came about in the late 1930's as a mix of Landau Theory and the Ginzburg criterion. This attempted to establish meaningful mathematical model for the phase transition that superconductors go through, without considering microscopic and subatomic effects. The general idea is to use the free energy of the system and its second order transition to show that it can be expressed as a complex order field, with parameter ψ. Classically it would reduce to zero at the transition, but with the complex portion, it becomes non-zero. This established the basis for two important parameters. The first is the Superconducting Coherence Length (ξ), which determines the scale on which small perturbations in the supercurrent density are allowed, without breaking the state. The second is the penetration depth (λ), which is linked to the Meissner effect and sets the scale over which external fields decay at the boundary of the superconductor. This also was used to determine the existence of two types of superconductors, Type-I and Type-II. Depending on whether the ratios of the length scales was less than or greater than $\frac{1}{\sqrt{2}}$. Type-1 fully expels external fields where type-II has a mixed state that allows some penetration.

Soon after in a 1957 paper "Microscopic Theory of Superconductivity"; Bardeen, Cooper, and Schrieffer developed what is now one of the most commonly used theories in superconductivity. BCS –Theory is used to interpret the majority of superconductors by taking the Ginzburg-Landau model a step further and using the microscopic interactions. They proposed that the superconducting state could be explained as a macroscopic quantum state. In this theory, the electrons condense from a fermion gas to a boson like state where the electrons are paired. These are known as "Cooper Pairs". This binding occurs based on a small attraction between electrons, caused by interaction with

2

phonons in the lattice as they pass through. In the superconducting state, this causes the paired state to have an energy level lower than the fermi energy of the system, effectively binding them.

Also in 1957, Alexi Abrikosov wrote "The Magnetic Properties of Superconducting Alloys" which introduced the concept of a supercurrent vortex inside type-II superconductors. This is currently called a fluxon (ϕ_0) and is a quantized amount of magnetic flux. All superconducting vortices will have the same total amount of flux, only varying sizes through different materials at different temperatures. This size is based on the characteristic lengths from Ginzburg-Landau Theory.

There was little progress in the experimental regime of superconductivity for the next few decades. Only a handful of new ones were found, and mostly were simply pure elements or Niobium with one additional. Suddenly, in the 1980s, there was an explosion in research associated with the field. Specifically, with Klaus Bechgaard synthesizing the first carbon based superconductor at the University of Copenhagen. This was the first real step toward producing complex superconductors with various non superconducting elements. This caused a massive surge with many material science groups testing all sorts of various composites. The first significant find was in 1986, when Bednorz and Muller published a paper "Possible high Tc superconductivity in the Ba−La−Cu−O system". Soon after that, there was the discovery of YBCO, the first "High Temperature" superconductor. It was found at the University of Alabama at Huntsville in 1987. Suddenly, the effect exists far above liquid nitrogen temperatures.

CHAPTER 2:
RELEVANT THEORETICAL BACKGROUND

This will only include the specifically relevant theoretical basis regarding the discussion and findings in the published work. First is the definition of some terms that exist throughout. Superconducting coherence length (ξ) is the length scale over which small distributions of super current are allowed to exist. It comes from Ginzburg-Landau theory and is defined as:

$$\xi = \sqrt{\frac{\hbar^2}{2m|\alpha|}} \tag{1}$$

Where $\hbar$ is the reduced Planck constant, m is the mass of the charge carrier (a cooper pair in this case), and α is a parameter from the Ginzburg-Landau field equations. The GL parameter is of particular interest here and how it changes near the critical temperature. There, it goes as:

$$\alpha(T) \propto \alpha_0 (T - T_c) \tag{2}$$

As we approach the critical temperature, the coherence length grows exponentially large. This is the main cause of the explosion phenomenon.

The Superconducting Penetration Depth (λ) also comes out of Ginzburg-Landau theory. This factor determines the length scale over which external magnetic fields can persist and decay into the body of a superconductor. It is defined as:

4

$$\lambda = \sqrt{\frac{m}{4\mu_0 e^2 \psi_0^2}} \tag{3}$$

Here, $\mu_0 = 4\pi \times 10^{-7}$ H. m^{-1} is the permeability constant, e is the charge of an electron, and ψ_0 is the value of the Ginzburg-Landau field parameter in the absence of an applied field. For clarification, the GL parameter is related to α and β as:

$$|\psi|^2 = -\frac{\alpha}{\beta} \tag{4}$$

These are combined to give the general Ginzburg-Landau parameter κ. This is the ratio of the two length scales and leads to the two various regimes with Type-I $\kappa < 1/\sqrt{2}$ and with Type-II $\kappa < 1/\sqrt{2}$

2.1 THE MEISSNER EFFECT AND LONDON EQUATIONS

Superconductors firmly within their condensed state experience a "perfect" diamagnetism. This phenomenon is called the Meissner effect (or Meissner–Ochsenfeld effect) named after the German physicists Walther Meissner and Robert Oschenfeld discovered it in 1933[13]. They found that superconductors below their critical temperature expel all external magnetic field. This was an accidental find because their measurement was of the external field. They found that the external field increased as all of the magnetic flux was pushed out of the sample, and packed tightly around the edges, increasing local field strength. This effect can be seen Figure 2.1.

5
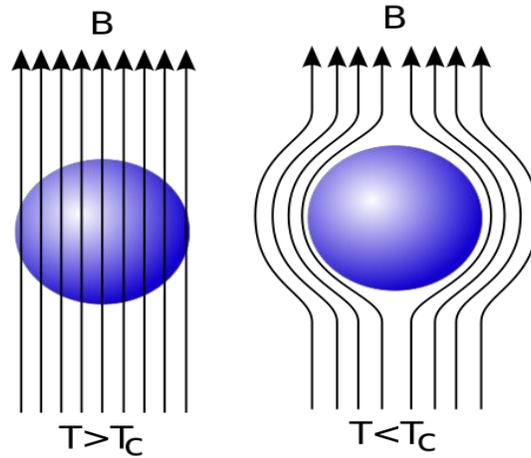
Figure 2.1 Material above (Left) and below (Right) the critical transition temperature

The first mathematical formalism for this effect came in 1935 from the London

Brothers (Fritz and Heinz). Their interpretation of the superconducting state using the

local electro-magnetic fields (E and B) along with basic qualities of the conductor (n_s and

J_d) is one of the simpler views on the subject and more classical in nature. The two

London equations can be shown:

$$\frac{\partial \boldsymbol{j}_s}{\partial t} = \frac{n_s e^{\wedge}2}{m} \mathbf{E} \tag{5}$$

$$\boldsymbol{\nabla} \mathrm{x} \boldsymbol{j}_s = -\frac{n_s e^{\wedge}2}{m} \mathbf{B} \tag{6}$$

The first equation is a basic force equation, but novel for the fact that includes no

limit on acceleration of the charge carriers (as long as the superconducting state is held).

This leads to a ballistic acceleration of charges through the superconductor as long as an

electric field persists. Where classically, Ohm's law says that there must be some long-

time dependent relationship between E and J (or V and I). This effect is studied further in

(Gabriel F Saracila, 2010)

6

The second equation regarding the magnetic behavior can be manipulated using Ampere's Law into a general Laplacian Field equation:

$$\mathbf{\nabla} \times \mathbf{B} = \mu_0 \mathbf{j} \tag{7}$$

$$\nabla^2 \mathbf{B} = \frac{1}{\lambda^2} \mathbf{B} \tag{8}$$

This implies a solution where:

$$\lambda \equiv \sqrt{\frac{m}{\mu_0 n_s e^2}} \tag{9}$$

So, the magnetic field inside the superconductor must decay exponentially with the rate set by λ:

$$B(x) = B_0 e^{-x/\lambda_L} \tag{10}$$

This comes out as the Magnetic Penetration Depth (λ). This sets the length scale over which this rapid exponential decay occurs inside a superconductor at the boundaries. This is the basis of the Meissner Effect. It also had a definitive dependence on the current distance from other critical parameters (T_c and j_d).

2.2 GINZBURG-LANDAU THEORY

This phenomenological theory was proposed in 1950, and is a special case of more general Landau Theory. In this case, the free energy (F) is thought as the functional of a generalized field that describes all possible phases and transitions. Introduced by Ginzburg and Landau, the order parameter Ψ is zero in the high temperature phase, outside the superconducting state and $\Psi \neq 0$ below Tc, when the state transitions. The

7

order parameter must contain information describing the new ordered phase. They postulate that Ψ is small and only slightly varies with position. Because of this, the theoretical model works best close to the transition temperature (Tc) where the order parameter is very small.

The difference between the normal and superconducting free energy in the presence of a magnetic field in a superconductor in terms of the order parameter |Ψ| is:

$$F_S - F_N = \frac{1}{V} \int d^3r \frac{1}{2m^*}[(-i\hbar\nabla + q^*A)\Psi^*(i\hbar\nabla + q^*A)\Psi + \tag{11}$$

$$+ \frac{1}{2\mu_0}B^2(r) - \mu_0 H(r)M(r) + \alpha\Psi\Psi^* + \frac{\beta}{2}\Psi\Psi^*\Psi\Psi^*$$

In small fields with low gradients we see the Free Energy Densities:

$$f_s - f_n = \alpha|\Psi|^2 + \frac{1}{2}\beta|\Psi|^4 \tag{12}$$

This free energy is minimized for

$$|\Psi|^2 = |\Psi_\infty|^2 = -\frac{\alpha}{\beta} \tag{13}$$

And when α<0<β. Here $|\Psi_\infty|^2$ is an "infinitely" large inside the bulk material. Including the presence of gradients and fields and writing Ψ = |Ψ|$e^{-i\phi}$ we get

$$f_s - f_n = \frac{1}{2m^*}[\hbar^2(\nabla|\Psi|)^2 + (\hbar\nabla\varphi - \frac{e^*A}{c})^2|\Psi|^2 \tag{14}$$

where the second term gives the kinetic energy associated with super-currents. In London theory is constant. Equating the second term of the equation with the energy density found by London we get:

$$\frac{1}{2}n_s m v_s^2 = \frac{A^2}{8\pi\lambda^2} = \frac{e^{*2}A^2|\Psi|^2}{2m^*c^2} \tag{15}$$

Leading to:

$$\lambda^2 = \frac{m^* c^2}{4\pi |\Psi|^2 e^{*2}} \tag{16}$$

Replacing $n_s^* = |\Psi(r)|^2$ the result agrees with the definition of the London penetration

depth, but the density, mass and charge values are now effective. Experimental results

gave that $e^* \approx 2e$, $m^* = 2m$, and $n_s^* = n_s/2$. With $|\Psi_\infty|^2 = n_s^*$ and equations (2.24),(2.25) and

(2.29), we find the Ginzburg-Landau parameters to be:

$$\alpha(T) = -\frac{2e^2}{mc^2} H_c^2(T) \lambda^2(T) \tag{17}$$

$$\beta(T) = \frac{16\pi e^4}{m^2 c^4} H_c^2(T) \lambda^4(T \tag{18}$$

$$|\Psi_\infty|^2 = \frac{mc^2}{8\pi e^2 \lambda^2(T)} \tag{19}$$

Solving the GL differential equations, expressions for the coherence length ξ and the

penetration depth λ are found. Most important, the Ginzburg-Landau parameter κ is

defined as

$$\kappa = \frac{\lambda(T)}{\xi(T)} = \frac{2\sqrt{2}\pi H_c(T) \lambda^2(T)}{\Phi_0} \tag{20}$$

With $\Phi_0 = \frac{hc}{2e} = 2.07 \times 10^{-7} G \cdot cm^2$ is a flux quantum. They found that the value

$\kappa = \frac{1}{\sqrt{2}}$ separates superconductors of type I and Type II.

2.3 BCS THEORY

Named after the founders in 1957 John Bardeen, Leon Cooper, and John Robert Schrieffer (BCS) was the first theory to discuss superconductivity in terms of small scale interactions as opposed to large scale field or wave states. Specifically, the carriers within a superconductor condensed into a superfluid of paired electrons (Cooper Pairs).

In London theory, the rigidity of the wave function would be ensured if the excited states of the superconductor were separated from the ground state by an energy gap, which explains also the anomaly in the specific heat. It took almost fifty years for the problem of superconductivity to be solved and explain the gap. In 1957, Bardeen, Cooper and Schrieffer established a new theory, which successfully explains superconductivity at temperatures close to absolute zero. Their theory is referred to as BCS theory.

This is seen to be on the order of around a few meV per electron. Such a gap is a relatively small effect (quantitatively) that yields a significant qualitative effect. Thus, the Coulomb correlation energy is larger and can be ruled out (if some effect is associated with an energy too large, then that effect is not the cause of superconductivity). If we change the isotope of which the superconductor is made of, the critical temperature changes. Spin-spin and spin-orbit interactions do not change with changes in the isotope, so they should be neglected. So superconductivity has something to do with interactions between electrons and phonons. In 1950, Frohlich [13] was the first in suggesting the importance of electron-lattice interaction that was confirmed by the discovery of the isotope effect [18] [19] , i.e., the proportionality of T_c and H_c to $M^{-1/2}$ for isotopes of the same element. In 1956, Cooper showed that even a weak attraction can bind pairs of electron into a bound state and the Fermi sea of

electrons is unstable against the formation of a least one bound pair, regardless of how weak the interaction is, so long as it is attractive. According to this theory, as one electron passes by positively charged ions in the lattice of the superconductor, the lattice distorts and the center of positive charge shifts. Virtual phonons are emitted and form a cloud of positive charges around the electron. After the electron passes, but before the lattice springs back to its normal position, a second electron is drawn to the cloud. It is through this process that two electrons, which should repel one another, get connected. As one electron of a Cooper pair passes close to an ion in the lattice, the attraction between them causes a vibration. This vibration can be passed from ion to ion until the other electron of the Cooper pair absorbs the vibration. The net effect is that the electron has emitted a phonon and the other electron has absorbed the phonon.

The Coulomb interaction among two electrons gives the interaction energy in space as:

$$V_c = \frac{4\pi e^2}{\left|\vec{k}_1 - \vec{k}_2\right|^2 + \lambda_{TF}^2} \tag{21}$$

in the Thomas-Fermi approximation, where $\lambda^2{}_{TF}$ is the screening parameter. Calling V the potential due to electron-phonon interaction, in order to get attraction, we need $V_c + V < 0$. It is more favorable if $\vec{k}_1 = -\vec{k}_2$.
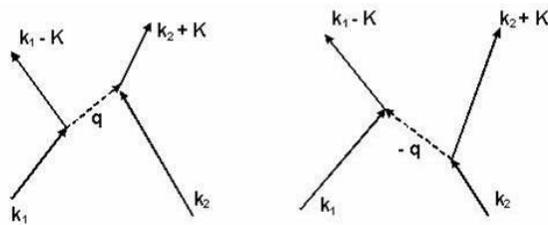

Figure 2.2: Two electrons processes mediated by phonons

11

With this, we write the Hamiltonian in k-space as:

$$H = \sum_K \epsilon(k)b_k^* b_k + \sum_{K,k_1,k_2} V(K)b_k^* b_k b_{k_1-K}^* b_{k_2+K} \tag{22}$$

Where the first term represents the kinetic energy of the electrons measured from the Fermi level and b^* and b are the creation and annihilation operators. The second term $V(K)$ is the electron-phonon interaction. Dealing with fermions, they must obey the anti-commutation relations $[b_k, b^*_{k0}] = b_k b^*_{k0} + b^*_{k0} b_k = \delta_{kk0}$ Canonical transformations introduced by Bogoliubov [32] show pairing properties i.e. they link the state (k^+) with the state (k^-).

These are:

$$\beta_k^* = u_k b_k^* - v_k b_{-k} \tag{23}$$

$$\beta_{-k}^* = u_k b_{-k}^* + v_k b_k \tag{24}$$

$$\beta_k = u_k b_k - v_k b_{-k}^* \tag{25}$$

$$\beta_{-k} = u_k b_{-k} + v_k b_k^* \tag{26}$$

Here u_k and v_k are the transformation coefficients and β_k, β_k^* have the same anti-commutation relations for fermions if $u_k^2 + v_k^2 = 1$. Using the anti-commutation properties and the fact that for the ground state: β_k (no objects in the "vacuum" can be annihilated) will lead to the new Hamiltonian at zero temperature:

$$H = 2\sum_k \epsilon(k)v_k^2 + \sum_{K,k} u_k v_k u_{k'} v_{k'} + \tag{27}$$

$$+ \sum_{k} \left\{ 2\epsilon(k)u_k v_k + (u_k^2 - u_k^2) \sum_{K} V(K)u_{k'}v_{k'} \right\} \beta_k^* \beta_{-k}^*$$

We make the third term equal zero (in order to find the energy of the ground state we choose u_k and v_k to eliminate this term which has the creation operators) and the BCS assumption that the attractive potential $V(K) = -V$ (constant) between an energy range $\pm\hbar\omega$. Now we define:

$$\Delta_0 \equiv -V \sum_{-\hbar\omega}^{\hbar\omega} u_{k'}v_{k'} \tag{28}$$

when $1 = u_k^2 + v_k^2$ yields:

$$u_k^2 = \frac{1}{2}[1 + \frac{\epsilon(k)}{\sqrt{\Delta_0^2 + \epsilon^2(k)}}] \tag{29}$$

and

$$v_k^2 = \frac{1}{2}[1 - \frac{\epsilon(k)}{\sqrt{\Delta_0^2 + \epsilon^2(k)}} \tag{30}$$

Substituting back in (2.16) gives

$$1 = -\frac{1}{2}V \sum_{-\hbar\omega}^{\hbar\omega} \frac{1}{\sqrt{\Delta_0^2 + \epsilon^2(k)}} \tag{31}$$

and changing the momenta into an integral over, we get

$$1 = -\frac{V}{2} \int_{-\hbar\omega}^{\hbar\omega} N(\epsilon) \frac{d\epsilon}{\sqrt{\Delta_0^2 + \epsilon^2}} \cong \frac{N(E_F)}{V} 2 \int_{0}^{\hbar\omega} \frac{d\epsilon}{\sqrt{\Delta_0^2 + \epsilon^2}} \tag{32}$$

so

13

$$\Delta_0 \approx 2\hbar\omega e^{-\frac{1}{N(E_F)V}} \tag{33}$$

for weak-coupling $N(E_F)V << 1$. This parameter Δ_0 represents the binding energy of

a Cooper pair. Going back to (2.15) we get:

$$\epsilon_0 = 2\sum_k \epsilon(k) - \frac{1}{2}\Delta_0^2 \sum_k \frac{1}{\sqrt{\Delta_0^2 + \epsilon^2(k)}} \tag{34}$$

The eigenstate $|0>$ has a lower energy than the full Fermi sphere of electrons.

This state is the vacuum of the operators β_k, β_{k^*}, according to its definition β_{k^*} creates

an electron in the state k with amplitude μ_k and at the same time destroying an

electron in the state $-k$ with amplitude v_k (hole). The excitations of the

superconducting state are thus rather peculiar quasi-particles which change from

being electrons to being holes as they pass through the Fermi level. In the range of

energy Δ_0 each quasi-particle is a mixture of an electron in k and a hole in $-k$. The

energies of these excitations are just

$$E(k) = \sqrt{\Delta_0^2 + \epsilon_k^2} \tag{35}$$

Even at the Fermi surface where $\epsilon_k = 0$, $E(k) = \Delta_0 > 0$. Δ_0 is the energy gap above

the superconducting ground state and the excitations consist of the breaking of pairs.

At finite temperature, the critical temperature is defined as the temperature at which

$\Delta(T)$ goes to zero. In this case E(k)➔ε(k), and the excitation spectrum becomes the

same as in the normal state. It leads to the famous BCS relation $\frac{\Delta(0)}{kT_c} = 1.764$.

The temperature dependence of the gap is found as $\frac{\Delta(T)}{\Delta(0)} \approx 1.74\sqrt{1 - \frac{T}{T_c}}$ for weak-coupling superconductors. In strong-coupling theory Δ becomes complex and energy dependent according to tunneling measurements.

2.4 ABRIKOSOV VORTICES

Vortices deserve special mention here, as a significant portion of our findings deal with their life and death cycles within the superconducting state. In a Type-II superconductor, some magnetic flux is allowed through the bulk of the material once an applied magnetic field surpasses the lower critical field limit (B_{c1}). The flux penetrates the material in small holes. In order to maintain this field, small portions of supercurrent circulate the "core" of the vortex. These were first predicted by Alexi Abrikosov in 1957 (Abrikosov, 1957).
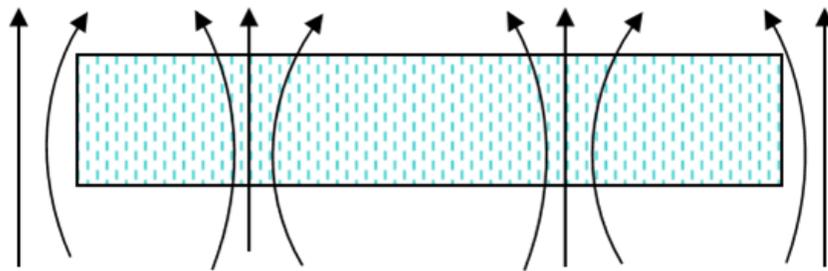

*Fig 2.3 Top-Down View of Vortices*
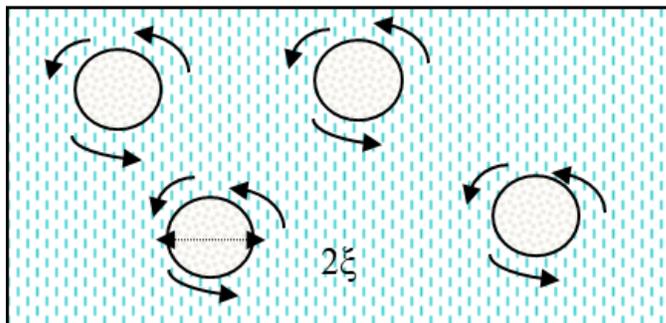
Fig 2.4 Side View of Vortex Cores

This creates a pockets of the quantum system pushed into the normal state, with small supercurrents circling around it to counteract the local field. These are Abrikosov Vortices and have an approximate core width equal to 2ξ. Also called fluxons, they are a quantized amount of magnetic flux given as $\phi_0 = {}^h/_{2e}$. This amount of flux is the same regardless of what material they exist in and permeate through. At the boundary of these vortices, there is a gradient of supercurrent density (n_s in the below figure 2.3.3) that increases as you go further from the core (r), at a rate based on the coherence length. The local magnetic field decays as you enter the superconductor.
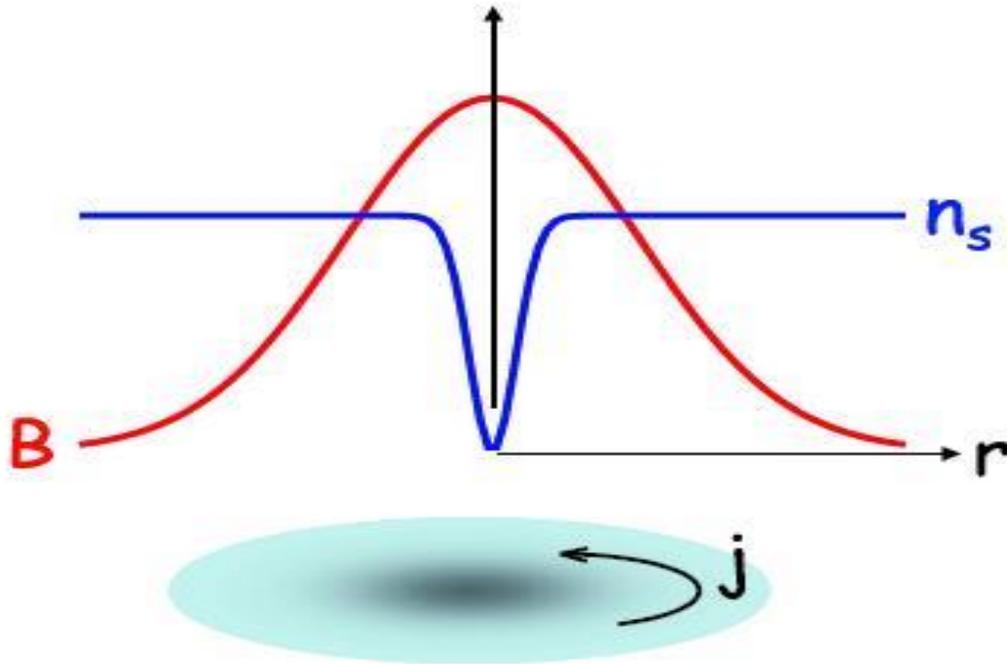

*Figure 2.5 Shows the relative qualities of the supercarrier density ns
and the B-field as how they relate with distance r from the center of the vortex core.*

This local field decays as a zeroth order Bessel function:

$$B(r) = \frac{\Phi_0}{2\pi\lambda^2} K_0 \left(\frac{r}{\lambda}\right)$$

(36)

$$\approx \sqrt{\frac{\lambda}{r}} \exp\left(-\frac{r}{\lambda}\right) \tag{37}$$

The field within the core is more generally shown as:

$$B(0) \approx \frac{\Phi_0}{2\pi\lambda^2} \ln \kappa, \tag{38}$$

Where κ is the Ginzburg-Landau parameter, and is greater than $1/\sqrt{2}$ for Type-II superconductors.

2.5 DISSIPATION FROM FLUXON INTERACTION

As previously discussed, much of the dissipation or resistance seen within the transition of Type-II superconductors comes from the interaction between the vortices and the current travelling through the superconductor. Although this was shown to be false by E Bruner Hansen, the force on the vortices looks just like a Lorentz force related by:

$$\mathbf{F}_{Lorentz} = \mathbf{j} \times \frac{\phi_0}{c} \tag{39}$$

As the current flows across the vortices, they receive a perpendicular acceleration that causes them to flow. This new movement creates a localized time variant B field and introduces Maxwell's equation for Faraday Induction:

$$\nabla \times \mathbf{E} = -\frac{\partial \mathbf{B}}{\partial t} \tag{40}$$

17

This motion creates an electric field opposite the direction of the current, or a reverse emf. As the reverse emf opposes the current and tracks proportionally with the applied current, it is seen as a resistance within the sample.

2.6 LIKAHREV CONDITION FOR VORTEX EXPLOSION

A novel phenomenon related to the Abrikosov Vortex was established by Konstantin Likharev in 1979 (Likharev, 1979). He proposed that these vortices can essentially "explode" if constrained too tightly. This condition is when the superconducting coherence length is on the same length scale as the boundary to which the vortex is constrained. Visually:
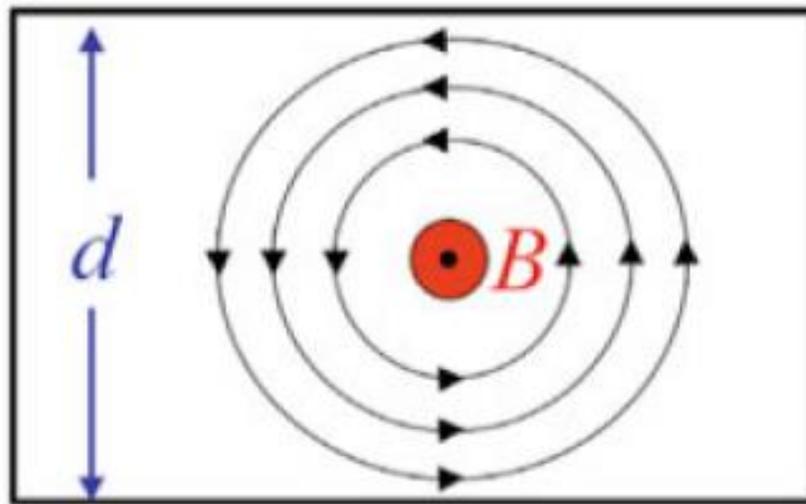
Figure 2.6 Shows the relationship between the confining dimension (d) and the effective width of the vortex.

In Figure 2.6, 'd' is the constraining width (in thin films, it's usually denoted as the thickness or depth of the film). As the size of the vortex approaches that of its container, the supercurrent required to maintain that magnetic flux is squeezed. As discussed previously, the coherence length is dependent upon the "strength" of the state. This state can be weakened by additional energy in the form of a higher temperature or a

higher local current density. So, as the super current is squeezed, the density grows, which increases the size of the vortex. This further squeezes the current and starts a feedback loop. This quickly leads to the phenomenon of "vortex core explosion". The condition for which this occurs is $4.4 \, \xi \leq d$.

2.7 BKT THEORY

2.7.1 GENERAL KT SUPERFLUID STATES

The Kosterlitz–Thouless transition (BKT transition) is a phase transition in the two-dimensional (2-D) XY model. It is a transition from bound vortex-antivortex pairs at low temperatures to unpaired vortices and anti-vortices at some critical temperature. Established by physicists John M. Kosterlitz and David J. Thouless. KT transitions can be found in several 2-D systems in condensed matter physics that are approximated by the XY model, including Josephson junction arrays and thin disordered superconducting granular films.

The XY model is a two-dimensional vector spin model that possesses U(1) or circular symmetry. This system is not expected to possess a normal second-order phase transition. This is because the expected ordered phase of the system is destroyed by transverse fluctuations, i.e. the Nambu-Goldstone modes (see Goldstone boson) associated with this broken continuous symmetry, which logarithmically diverge with system size. This is a specific case of what is called the Mermin–Wagner theorem in spin systems. Rigorously the transition is not completely understood, but the existence of two phases was proved by McBryan & Spencer (1977) and Fröhlich & Spencer (1981).

In the XY model in two dimensions, a second-order phase transition is not seen. However, one finds a low-temperature quasi-ordered phase with a correlation function

(see statistical mechanics) that decreases with the distance like a power, which depends on the temperature. The transition from the high-temperature disordered phase with the exponential correlation to this low-temperature quasi-ordered phase is a Kosterlitz–Thouless transition. It is a phase transition of infinite order.

In the 2-D XY model, vortices are topologically stable configurations. It is found that the high-temperature disordered phase with exponential correlation decay is a result of the formation of vortices. Vortex generation becomes thermodynamically favorable at the critical temperature Tc of the KT transition. At temperatures below this, vortex generation has a power law correlation.

Many systems with KT transitions involve the dissociation of bound anti-parallel vortex pairs, called vortex–antivortex pairs, into unbound vortices rather than vortex generation. In these systems, thermal generation of vortices produces an even number of vortices of opposite sign. Bound vortex–antivortex pairs have lower energies than free vortices, but have lower entropy as well. In order to minimize free energy, F=E-TS, the system undergoes a transition at a critical temperature, Tc. Below Tc, there are only bound vortex–antivortex pairs. Above Tc, there are free vortices.

The thermodynamic argument for the V-aV pair creation regime. Given the energy of a vortex is $E_0*\ln(R/r)$. Here E_0 depends on the system which the vortices are created, R is the limiting size of the system (smallest of l,w, OR d) and r is the size of the vortex ($\sim\xi$). In the 2-D planar system, the number of spacial states (N_x) goes as $(R/\xi)^2$. The entropy then goes as: $S=k_B\ln(N_x)$.

$$S = k_B T \ln(Nx) = 2k_B T \ln\left(R/\xi\right) \tag{41}$$

Inserting into the Free Energy Equation:

$$F = E - TS = \mathrm{E}_0 * \ln\left(R/\xi\right) - 2k_B T \ln\left(R/\xi\right) \qquad (42)$$

$$F = (\mathrm{E}_0 - 2k_B T) \ln\left(R/\xi\right) \qquad (43)$$

So, when the free energy is greater than 0, it is not energetically favorable for V-aV pairs to form. However, when F<0, it is statistically favorable for their generation. The junction at which they will or will not form can be found at $F = 0$:

$$F = (\mathrm{E}_0 - 2k_B T) = 0 \qquad (44)$$

$$\frac{\mathrm{E}_0}{2k_B} = T \equiv T_V \qquad (45)$$

We define this as T_V, which is the lower bound of the BKT region.

2.7.2 BEREZINSKII–KOSTERLITZ–THOULESS TRANSITION (BKT)

The BKT transition is a specific application of the more general KT superfluid vortices then applied to superconducting systems of similar context. The main system concerning our research is a 2-D virtual superconducting layer at the interface between a topological insulator and Chalcogenide. In this two dimensional system, we see these Vortex-antiVortex (V-aV) pairs statistically generated based on the favorability of their energy states and the thermal fluctuations in the material.

Above the BKT region, the superconductors will be normal, therefore no vortices will form without some condensed carriers formed. Within the BKT region, the carriers have condensed to form the superconducting state and there is enough energy to thermally unbind these pairs. As we track below some lower bound T_{BKT} the V-aV pairs are still thermally generated, however there is not enough free energy to thermally unbind them. Since dissipation in Type-II superconductors is generally the result of interaction

with fluxon vortices, we will see dissipation (resistance) effects within the regime that do not follow traditional theoretical models.
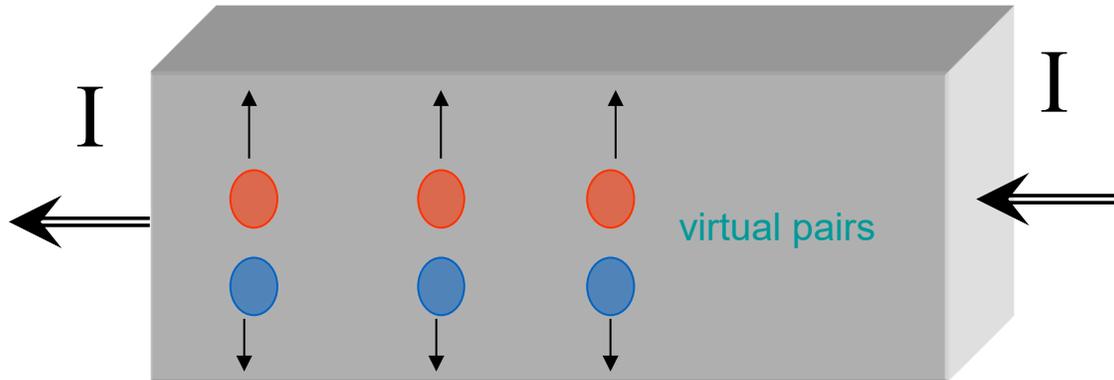

Figure 2.7 While in the BKT transition, virtual Vortex-antiVortex pairs are statistically generated AND thermally unbound

These virtual pairs, when unbound and subjected to an applied current, will move based on effectively a "Lorentz Force" law as previously discussed. This means in the unbound state we have additional measured dissipation. When the pairs are bound, below the BKT transition, they do not create this dissipation. Upon reaching the edge of the substrate they are either destroyed due to an inability to keep up the circulating supercurrent or are simply annihilated through collision with other vortices. These virtual pairs always exist below the BKT transition level, and are thermally activated. However, as we will discuss later, they can also become unbound through applying a "depairing" current to the system.

CHAPTER 3
INTERFACIAL SUPERCONDUCTIVITY AND BT/FT

The particular system in our experiment is a layered superconductor. There is a layer of bismuth telluride, which is itself a topological insulator, and a layer of iron telluride, an iron chalcogenide. While neither one independently is a superconductor, there is a manifestation of superconductivity at the interface between a topological insulator and an iron-chalcogenide compound. This is a very curious phenomenon, and helpful for probing many recent theoretical predictions surrounding these two, very new classes of materials. Our collaborators report electric transport measurements on a Bi_2Te_3/FeTe heterostructure that was fabricated using van der Waals epitaxy.
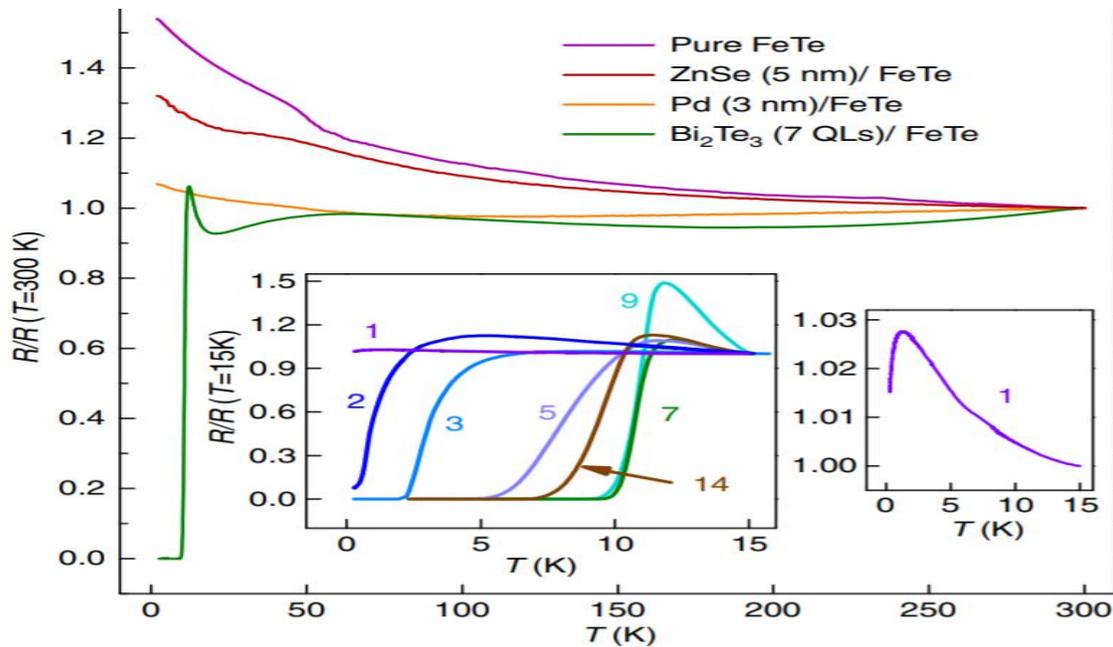

Figure 3.1 Electronic Transport measurements of the individual components of the system as compared to the Interfacial System

Induced by the BiTe epitaxial layer, the combination revealed superconductivity, with thicknesses even down to one quintuple layer. Though there is no clear-cut evidence that the observed superconductivity is induced by the topological surface states. The two-dimensional nature of the observed superconductivity with the highest transition temperature around 12K was verified by the existence of a Berezinskii–Kosterlitz–Thouless transition and the diverging ratio of in-plane to out-plane upper critical field on approaching the superconducting transition temperature. With the combination of interface superconductivity and Dirac surface states of BiTe, the heterostructure studied in this work provides a novel platform for realizing Majorana fermions. (Qing Lin He, 2014)
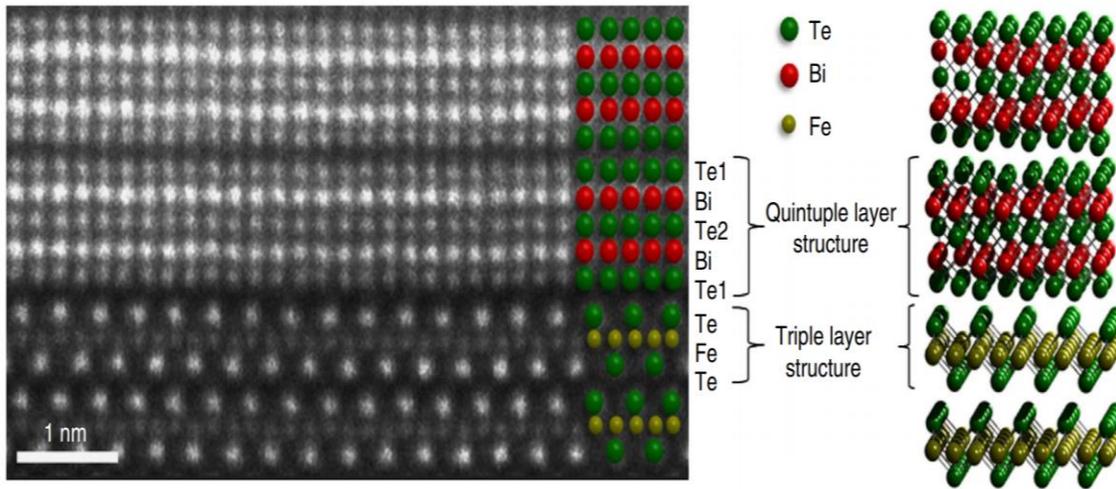

Figure 3.2 HADDF image showing the sharpness of the gap between the two layers
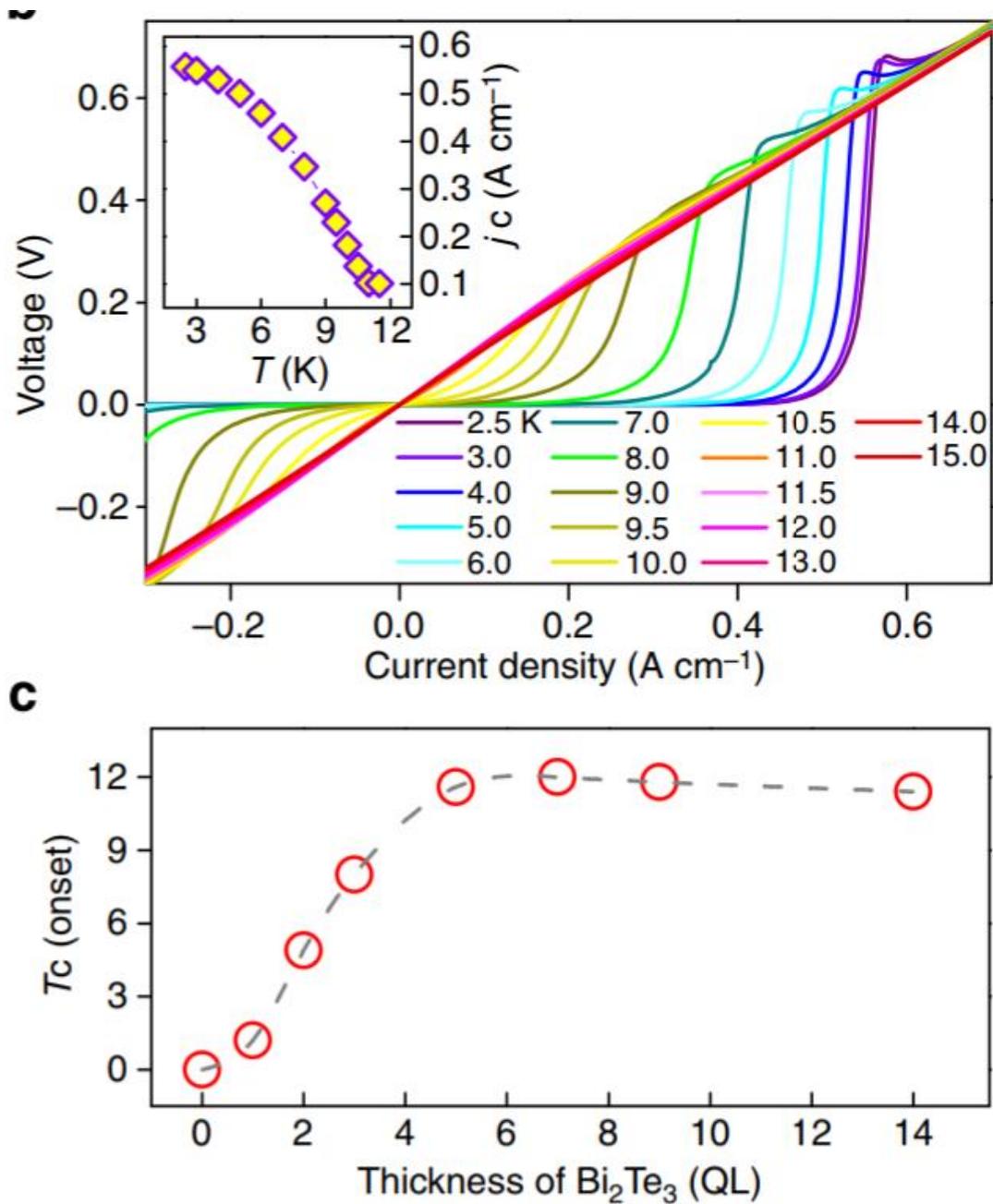
Figure 3.3 (Top) Current density dependent voltage of the Bi2Te3(7 QLs)/FeTe heterostructure at different temperatures. The inset shows its temperature-dependent critical current density. (Bottom) Tc(onset) versus the thickness of Bi2Te3 thin film in units of QL. The dash line is a guide to the eyes
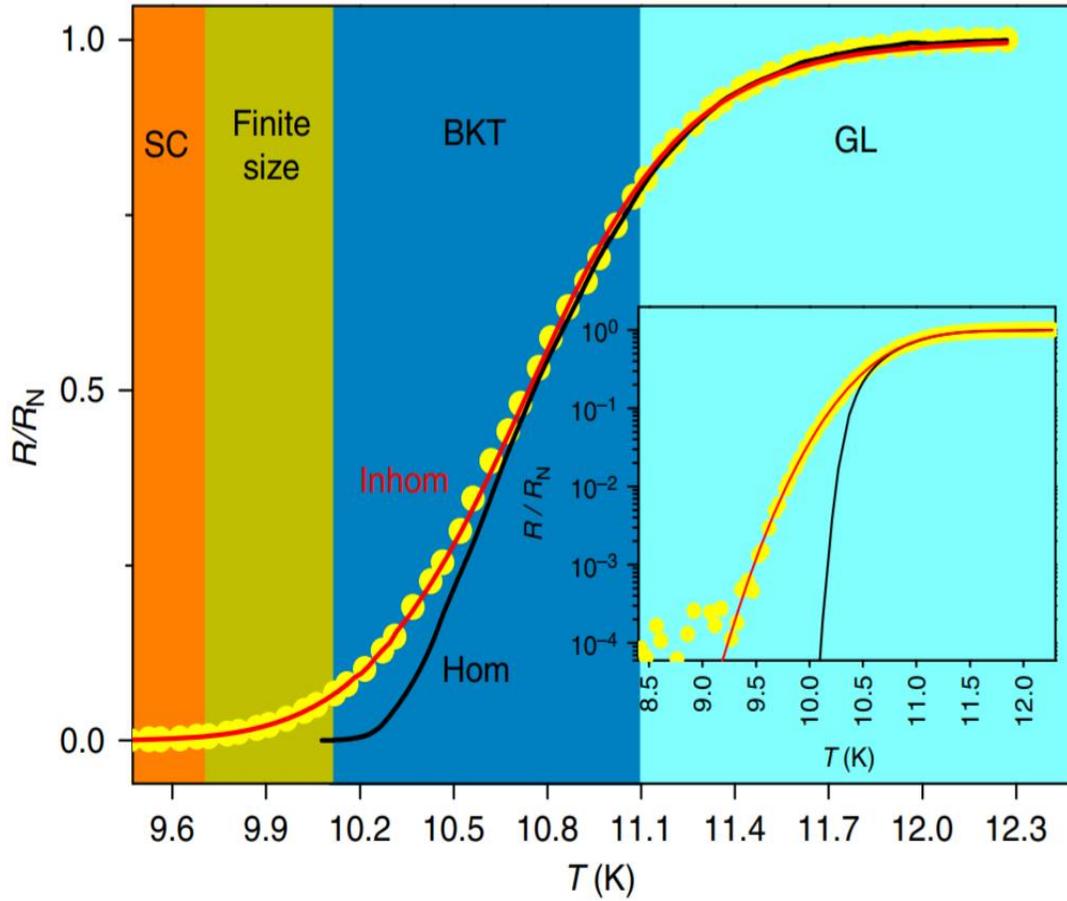
*Figure 3.4 The normalized R–T curve of Sample A is plotted in four regions covering from GL, BKT, FSE to SC. The inset shows the same curve in a logarithmic plot. The red curve is a fit with the interpolating an inhomogeneity effect model, while the black curve is a fit based on the infinite-size limit.*

CHAPTER 4
EXPERIMENTAL SETUP AND PROCEDURE

4.1 SAMPLE PREP

4.1.1 PHOTOLITHOGRAPHY

The first step in the photolithography was applying a layer of photoresist. For this, we used a simple dropper to apply photoresist AZ-1350JF on top of a cleaned sample. Then, a spin coater WS-650SZ-6NPP/LITE from Laurell Technologies Corp 4.2 was used to thin the drop into a layer for lithography. The spinner is compact and packed with advanced features like programmable/storable speed control, high-performance drive up to 12,000 RPM. It uses pressurized air to drive the pneumatic vacuum generator and protect its motor. A similar operation was used to create the specialized masks we made for this experiment.

Spinner Operation

1. Turn on the power supply of the spinner and compressor.

2. Make sure the outlet pressure of the compressor is in the range of 60 ∼ 70psi.

3. Press "Select Process" and use the up-down buttons to choose the saved set up process or create a new one.

4. Press "Edit Mode". Check all the settings. If you want to modify, press "tab <" and then move the flashing cursor to choose the parameter to change.

5. Press "Run Mode". Confirm the settings.

Figure 4.1 Spin Coating Machine

6. Open the lid and mount the right vacuum chuck. The 3mm chuck is a good choice for the sample. For the slide, the specific chuck should be used.

7. Put the sample or slide on top of the chuck. Carefully align the center of the sample at the rotational axis of the platform.

8. Press "Vacuum". The Vac reading on the screen should rise from 0 to about 23. If not, check the compressor and the contact between the chuck and sample. If the O-ring of the chuck is leaking, replace it.

9. Drip the photoresist or other chemicals on the top of the sample. Make certain that the chemical covers the whole surface without any bubbles. None of the chemicals should get into the hole of the chuck. If that happens, it may damage the motor. Therefore, it's very important to confirm the vacuum in last step to make sure the seal is good.

10. Close the lid.

11. Now the LED of the "Start" button should be illuminated.

12. Press "Start". The rotation will start. Wait for it to finish. If something goes wrong, press "Stop".

13. After it stops, open the lid.

14. Press "Vacuum". The Vac reading drops down to 0.

15. Take out the sample.

16. If finished all the coating, put a protecting cap on the chuck and close the lid. Turn off the power supply and the compressor.

4.1.2 PATTERN EXPOSURE

After coating the samples, we used the Olympus DP-11 microscope system in order to expose the photoresist. We used various masks to pattern our bridge (Figure 4.2), contact pads, and delineate everything. I rewrote the process in order to optimize sample stability and minimize the amount of handling/etching time required. The general process is as follows:

1. Prepare the developer (AZ-400K) bath, water bath, and drying station.

2. Insert main bridge pattern into the appropriate slot, centered in view finder.

3. Focus the pattern such that its edges are focused and then zoom in just a bit.

4. Remove protective UV and yellow filters from the microscope.

5. Expose main bridge pattern by turning up the intensity of the bulb, slowly, until reaching maximum.

29

6. Expose this pattern for approximately ¼ of the required time (e.g. for a 20x exposure that usually takes ~45 seconds, so 10-15 seconds).

7. Restore filters and transfer to development.

8. Develop pattern for approximately ¼ the required development time (for single coating, this is about 5 seconds).

9. Using this faint outline of our pattern, return to the microscope for exposure.

10. Using the various other slides and shields, delineate the main contact pads (more discussion in Appendix 1) by exposing for the full required duration.

11. Develop delineation for ~½ time.

12. Return and expose full pattern.

13. Develop until the pattern is fully visible.

14. Bake remaining photoresist pattern for an additional two minutes to strengthen the resist.

This process allows the delineating lines to be over exposed and weakened compared to the bridge pattern. When ion-milling, this helps guarantee isolation of the various contact pads and connections to the sample. I found the resist would often break down under etching and this seems to have corrected the issue.
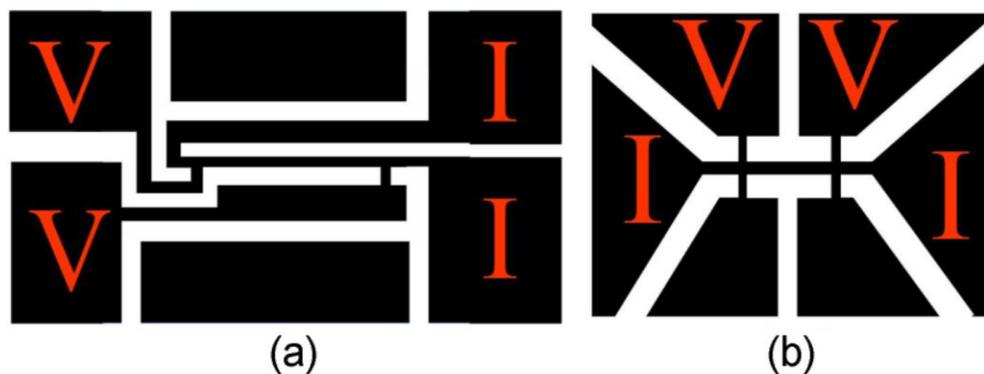
Figure 4.2 Schematics of our two more commonly used bridge geometries

4.1.3 ION MILLING SYSTEM

When the sample has been properly exposed, we move on to etching the pattern.

We do this by inserting it into our Ion Beam Milling System (IBMS-100). It injects

Argon gas into an evacuated system. It has an up to ~2.5keV energy beam that it uses to

bombard the sample with a variable current, useful in the range of 80-120uA. The

required strength of the beam depends on the toughness of the material being etched. It is

imperative to test the system to determine the lowest useful energy, as too much beam

energy can break down the injection needle, bias plates, or photoresist. After determining

the required energy, the argon injection rate can be adjusted to maximize the milling rate

for that particular energy.
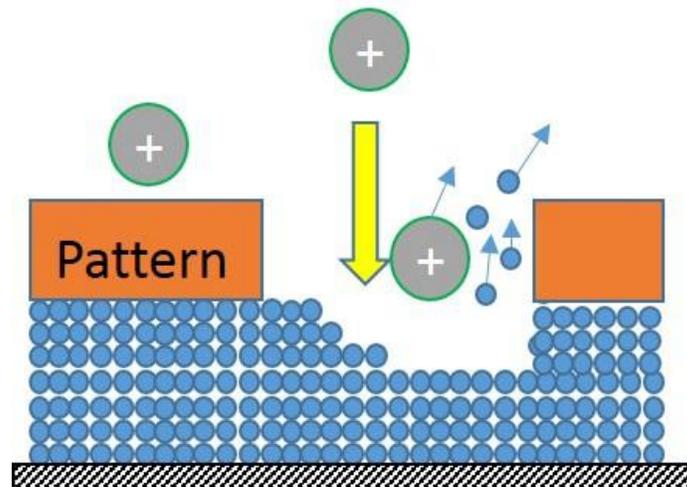
*Figure 4.3 Argon atoms bombard the film after accelerating through High Voltage plate.
The unprotected part will be etched and the parts with photoresist will remain intact.*

This process is preferable to other methods like acid etching because it reduces

undercutting and is generally safer due to the non-interactive nature of the Argon gas and

vacuum which etching is done in. One drawback is that the process can heat the sample

(ranges 15-25K) so any films with temperature sensitivity may not be optimum. Our procedure is as follows:

Operation for Oxford ion gun

1.   Make sure everything is at off position. The flow control valve should be at 0 and the green knob should be open. The lid of IBMS-100 should be also closed.

2.   Carefully put the sample at the marked position inside ion milling chamber.

3.   Mount the gun head with matching the marker positions at both ends.

4.   Turn on the rough pump.
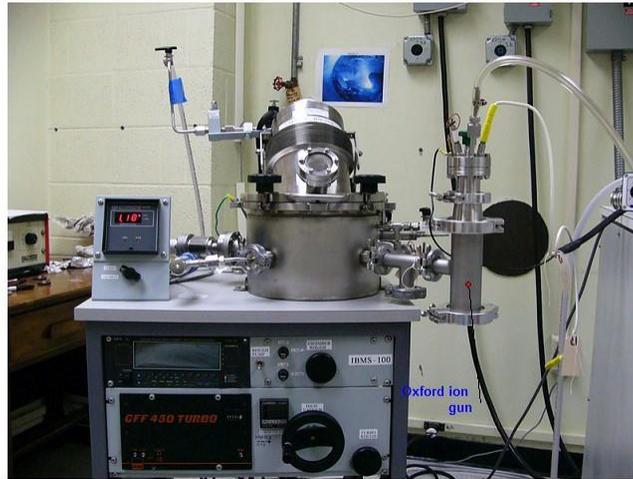
Figure 4.4: Oxford ion gun and IBMS-100

5.   Open the turbo rough valve fully.

6.   Switch the vacuum gauge to turbo position and monitor it. Wait for it to drop under 20 mTorr.

7.   Turn on the turbo pump. Push the switch "ON" and it will return to middle. At first, the yellow LED is on. When the green one in on after about 2 minutes, that means the turbo pump is in full speed. The turbo should be used only under full speed.

8. Fully close the turbo rough. Pay attention here. The panel is not flat so the knob may touch the panel when it's closing. Go for one more turn when it has touched the panel.

9. Open the chamber rough and switch the vacuum gauge to chamber position.

10. Let it drop to under 100 mTorr.

11. Close the chamber rough and switch the vacuum gauge again back to turbo.

12. Open the turbo rough again. Wait the reading drop back to 20 mTorr.

13. Check the chamber pressure and make sure it's less than 1000 mTorr. If not, make sure it's not leaking or repeat pumping the chamber by the rough pump with closing the turbo rough.

14. Slowly and carefully open the high vacuum valve while monitoring the turbo back end vacuum. It should not be over 100 mTorr.

15. Let it pump for about 20 minutes.

16. Open the argon gas cylinder and switch the manifold (Fig. 4.5) to old ion gun. Adjust the low pressure gauge to be 10 psi.

17. Set the flow control valve to be 6.1. Wait about 20 minutes to let the pressure to be stable.

18. Make sure the beam probe has been connected to the gun head. Turn on the power of the ion gun.

19. Adjust the beam current. The beam current should be able to reach $100\mu A$ with the beam energy less than 2.5keV. Never use higher energy. It's normal if the current is less than expected at the beginning since it usually will rise after it's heated up. If it failed to reach $100\mu A$, check the pressure. Adjusting the high vacuum valve may be helpful.

20.   When it's done, turn off the ion gun power supply. Close the gas cylinder and the flow valve.

21.   Close the high vacuum valve. Now it's ready to vent the chamber.

After the above procedures, the pump station is still on with turbo pump at full speed, turbo rough open and the following valves closed: chamber rough, high vacuum and flow control valve. To completely shut it down, the turbo pump should be turned off first and then the rough pump should run for another half hour to let the turbo pump slow down; it should also be cooled down by fan. Then close the turbo rough. It's ok to shut down the rough pump now. However, if it's necessary to take another ion milling soon, it's better to keep the turbo running. To do one more ion milling, just start from Step 7. (Liang, 2013)

4.1.4 APPLYING CONTACTS

Arguably the most intense step, applying contacts to these samples is like performing open heart surgery on a Lilliputian...with a toothpick. The most common way of applying wires to microbridge samples is using a contact wire bonding setup, often using wires made of Aluminum. We found this problematic as it can drastically increase contact resistance (orders of magnitude larger than the resistance of the bridge itself), can potentially damage the material (arms are often sharp and lead to fine cracks in some crystals), and the connections are easily disturbed or broken.

Instead, we use Indium as a bonding agent. It is very soft and reduces damage to the sample itself. As it does create a chemical bond with most metals, indium contact resistance is less than an Ohm (some in the mOhm range). We place copper wires within indium pads on the sample and have particularly low resistances along with solid

34

physical connections. One drawback from this process is that there are multiple junctions (Sample-Indium-tin-copper) that can introduce thermal offset voltages.

Figure 4.5: Size comparison of my wedding ring to size of contacts (tiny dots)

4.2 MEASUREMENT SYSTEM

4.2.1 PT 405 CRYOSTAT

The detailed diagram of PT405 cryostat and magnet is in Figure 4.6. PT405 is a two stage pulse tube cryocooler. It works with Cryomech CP950 compressor which requires water cooling to function. When it's running, the helium is compressed and then expands in the cold head. The expansion first happens in first station that will also cool down the gas and then in the second stage to drop the temperature lower. Therefore, the two stage cryocooler can provide lower temperature, but the path of the gas running through will be longer and so the frequency of compression and expansion will be lower (~ 1.4Hz). This results in the fluctuation of the temperature.

To get the temperature stable, we have to use the sound trigger system in Sec. 4.2.3.
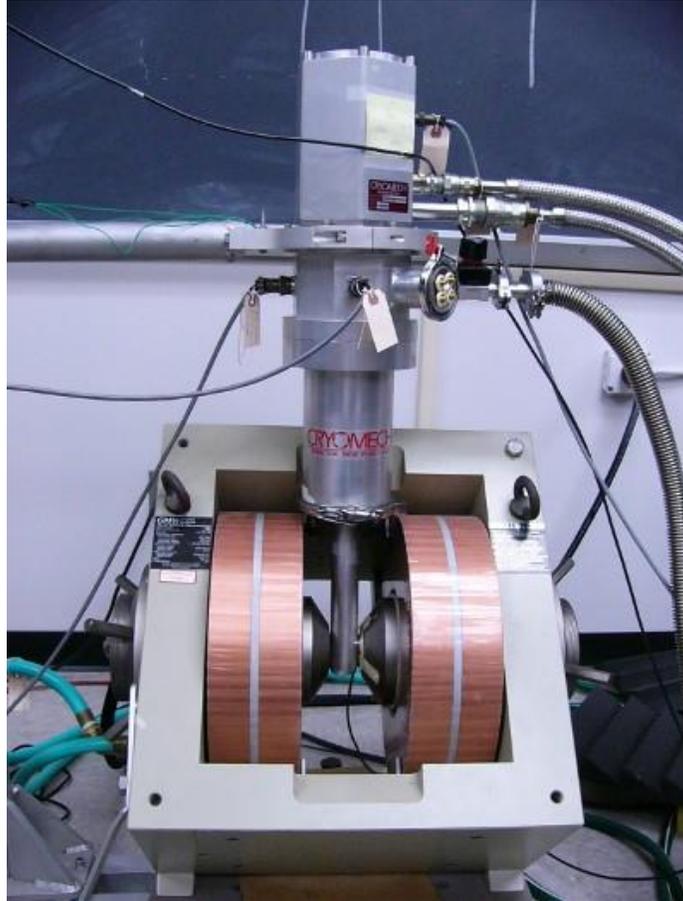

Figure 4.6: PT405 cryostat with GMW 3473-50 magnet.

The water cooling GMW 3473-50 magnet is installed on a rotor. It can be turned horizontally. Two ferromagnetic iron cores can be pulled out while mounting the sample. The maximum field is about 1.25T. One Hall magnetic sensor is placed on one of iron pole face to measure the field strength between the iron faces. The sample holder is on the end of an extension copper rod from the second stage of the pulse tube. The holder is also in between the magnet poles so that it changes the applied magnetic field on the superconductors.

36
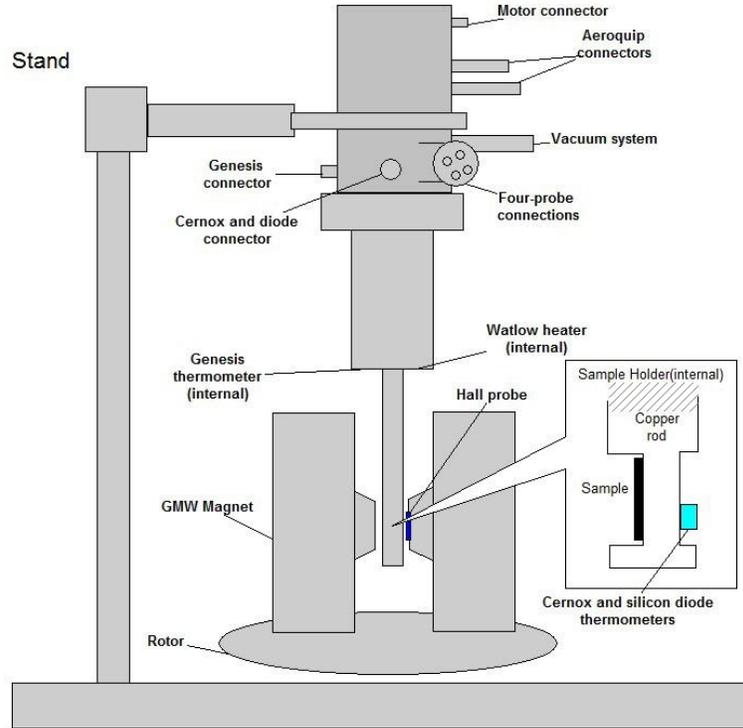
Figure 4.7: Schematic of PT405 and its magnet. The inset is the sample holder. The internal positions of sensors and heater are also present.

By choosing different sizes of copper plates, we can adjust the cooling power from the cooling stage to the top copper plate. Our goal is to use a 50W heater to heat up the top plate and change the temperature at the sample platform as well. To calculate the length required of the bottom copper plate, we start from the heat conduction formula:

$$q = -k(T1 - T0)/d \qquad (46)$$

where q is the heat flux and k is the thermal conductivity coefficient. For OFHC copper, $k \simeq 300W \cdot m^{-1} \cdot K^{-1}$ at 100K. T_1 and T_0 are the temperatures at two ends.

4.2.2 GMW MAGNET

For applying external magnetic field to the sample, we use GMW electromagnet, model 3473-50, was used to generate the magnetic field at the sample. The sample was

placed between two poles of 150 mm diameter; the gap between poles was around 35 mm. Figure 6.9 shows a picture of the magnet. A Power Ten, model I62B-4050A provides power to the electromagnet. The maximum current is 50A resulting in a field of around 1.3 Tesla.

An HGT2100 Hall probe was used to measure the magnetic field at the sample. A fixed dc-current of 1.008mA was sent to the Hall probe. The transverse voltage was measured by a Keithley model 2000 multimeter. It gives the transverse resistance, which is proportional to the magnetic field. The proportionality coefficient of our hall probe is ~194 Ohms/Tesla. The Hall probe's offset was calibrated using Helmholtz coils. The transverse voltage of these, as the current in the coils is increased, is given in Figure 6.10. The offset was found to be 0.75mV. So B is calculated using the formula:

$$B = \frac{V_{transverse}}{194 \cdot I_{longitudinal}} \tag{47}$$

The magnetic field remained consistent and very stable during all measurements. It gave a standard deviation around of 6.5×10^{-5} T (Gabriel F Saracila, 2010) . The profile of the field in the area of the sample probe can be seen as following:
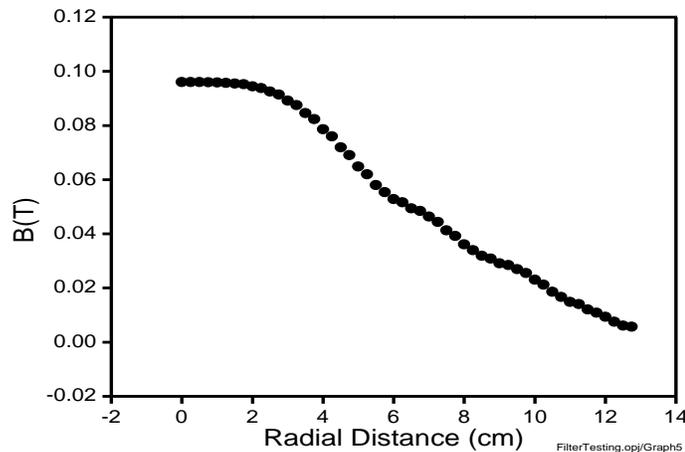

Figure 4.8 Radial Field Profile

38

Here we see the field as a function of the radial distance from the center of the two poles. The field has no real variance within the two poles (maximum variance of less than 1 cm from center). The transverse B-field profile was similarly well behaved. The maximum B variation is <1% and is much less in the sample area (+/- 0.5cm).
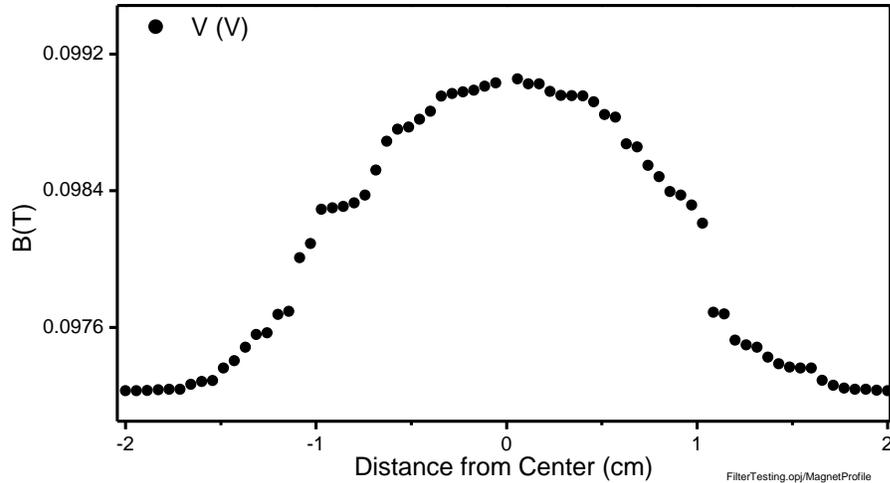

Figure 4.9: Longitudinal Field Profile

4.2.3 TEMPERATURE CONSIDERATIONS

Accurately measuring the temperature is the most difficult and important measurement for a variety of reasons. One of the most common issues comes in to play due to the pulsed nature of the cryostat cooling. Because our system "breathes" at a frequency of ~1.4Hz, this means there will be short term temperature fluctuations with a periodicity on that order. To combat this, we designed the system to have a significant amount of heat sinking, thermal isolation, and triggering based on this breathing cycle.

To help keep as much heat out of the system, there are concentric layers of aluminum and steel to help keep radiative heat transfer to a minimum. We also set the sample location to be on a significant amount of copper sinking and far away (0.5M)

39

from the tug of war between the cold head and the power resistor used to heat the chamber. This acts as a capacitor of heat energy which diminishes the fluctuation considerably.

In order to further minimize the effect of this temperature fluctuation, we have synchronized our measurement system to the breaths of the compressor using a very simple microphone setup. We listen to the sounds and delay our entire system's measurements based on how far into the cycle is optimum. The best delay depends on many properties of the sample and should be done empirically whenever a new material is used.
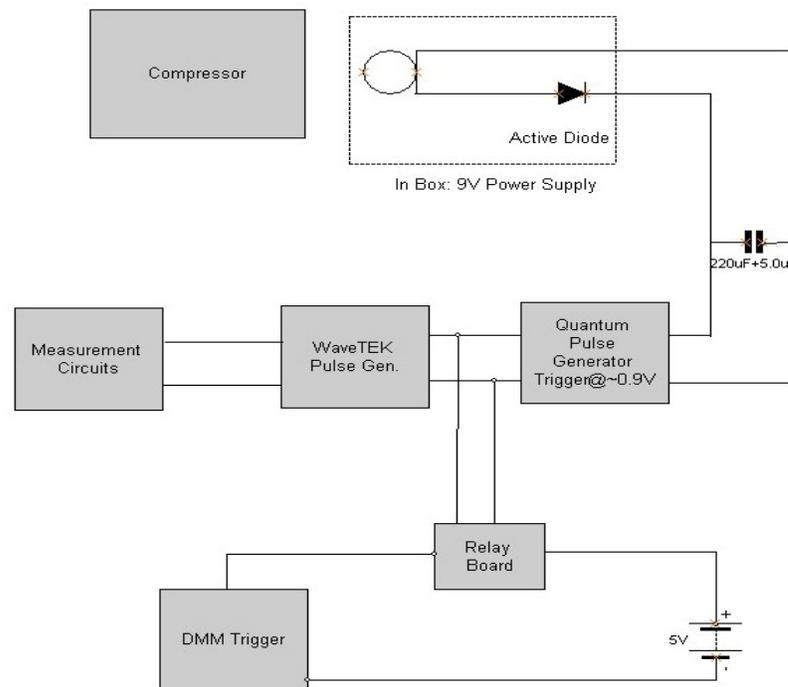

Figure 4.10: Trigger by Sound diagram

Another consideration was long term temperature instability. Though our current setup allows us to negate short term variation in temperature, there was significant long term drift associated with our setup. Because the temperature is "set" by changing the

40

power sent to our heater controller, this allows for long term swings in temperature just based on ambient room temperatures and the cooling power of the compressor (affected by the temperature of the water that is cooling it). Shown here, is a two day run where we were attempting to measure something at the same temperature (long slow RvsB):
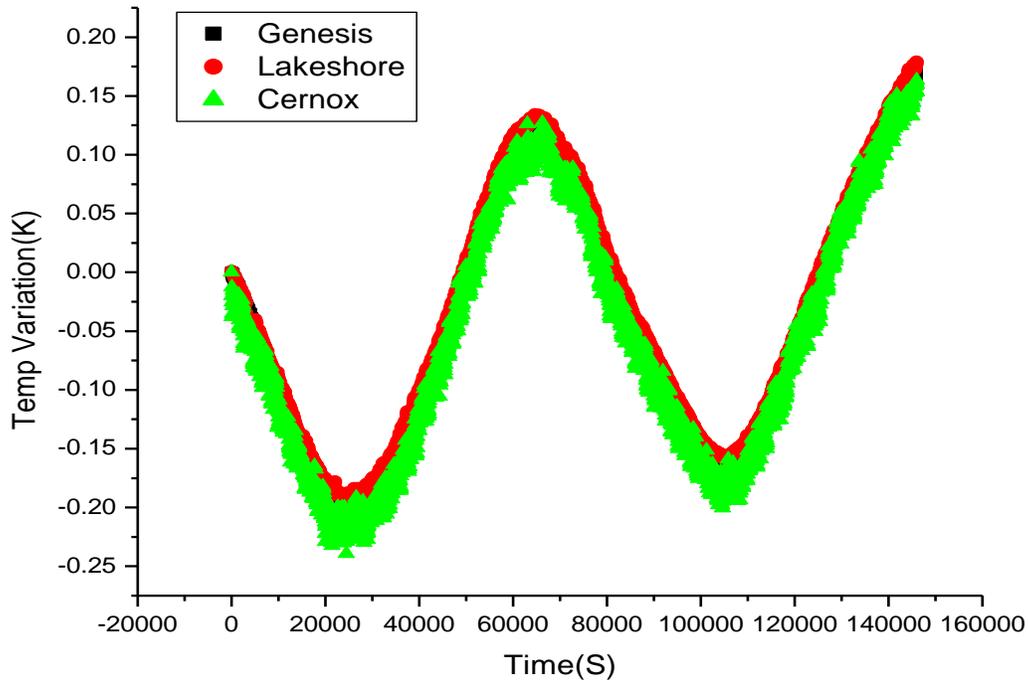

Figure 4.11: Long-term Temperature Instability

In order to correct for this, I wrote a temperature control program (Appendix B) in order to stabilize long term random shifts in cooling power. Essentially, it takes a weighted average of the most recent points, finds the general dT/dV of the heater and adjusts according to how far away from the temp it should be. This not only helps cancel out long term shifts, but the implementation specifically rejects large overcorrections. So, there is some very minor short term variance increase, but the long term effects are

41

considerably more helpful. Here, on the same relative scale, is the temperature shift after the correction program was tuned:


ChasesTempAdjustment.opj/Graph9
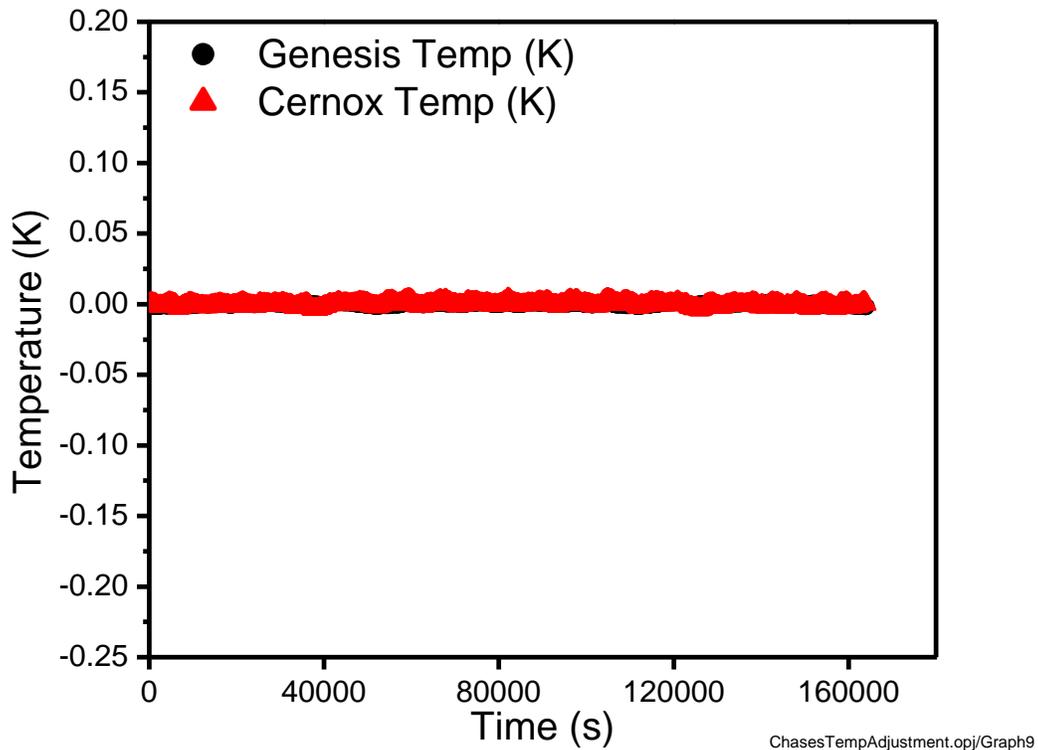
Figure 4.12: Corrected Temperature Control

4.2.4 DC MEASUREMENT

We use a very simple 4-probe measurement technique. There is a voltage source that flows into some large-variable ballast resistor to stabilize the current. Then it flows through a large standard resistor (~10,000 Ohms) for which we know the resistance to be stable and precise. Then it flows down the mounting platform to our sample and back to the supply. One addition that many people overlook is our use of a current reversal relay system that allows us to measure the current/voltage relationship in both directions. This is helpful because there are often significant voltage offsets (mostly thermal emf) that can be discarded by looking at the forward-reverse currents.
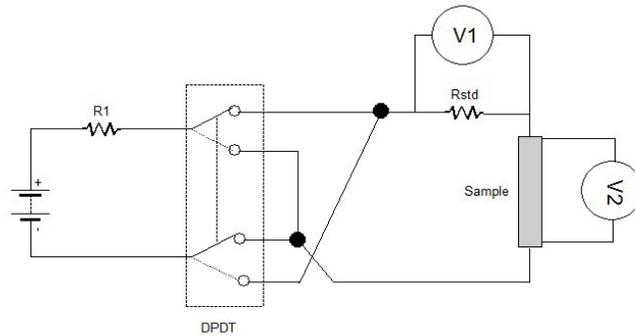
Figure 4.13: Circuit of DC 4-probe measurement. The Double Pole Double Throw(DPDT) relay is operated by the DAC card in the computer.

In this experiment, we were working with a very thin sample, and so wanted to extend our lower current measurement capabilities. One way we accomplish this is by using a buffer system within the Keithley meters themselves. We take repeated readings that are stored and then averaged by the meters themselves in order to minimize the amount of random fluctuation in the voltage signal.

This did not appear to be quite enough to get into the nA range like I had wanted. So, I designed a simple filtration circuit to help stamp out high frequency noise and stabilize the signal. Made more difficult because of the current reversal portion, simply throwing capacitors on there was not an option because the voltage needed to be able to respond fast enough to the switch. Here is an oscilloscope scan of the noise level that we started with:
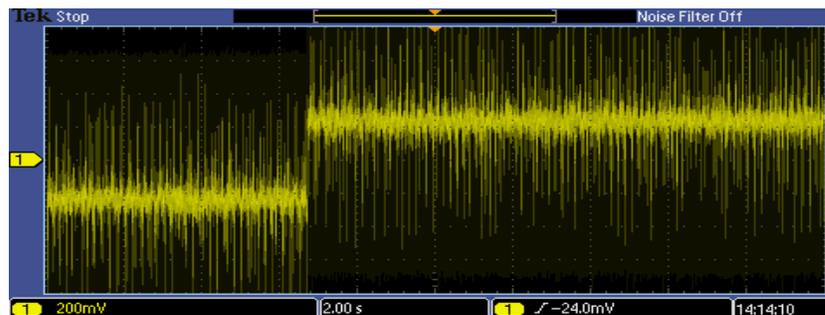

Figure 4.14: DC signal noise pre-filter

The jump in the middle of Figure 4.14 is the current switching directions, so the total signal size here is approximately 250 mV with noise at +500mV. This is a demonstrable set to show the noise to already be quite high (need levels 5-6 orders of magnitude lower), even at low signal levels (applied current is ~10uA). After some calculation and testing, the circuitry I came up with is shown here:
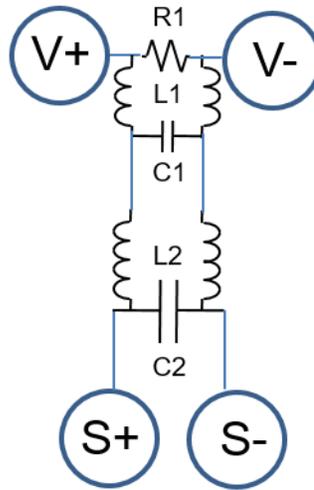

Figure 4.15 RLC Circuit with values R1=7Mohm, L1=.13mH, C1=50nF, L2=RFChoke, C2, 0.5uF
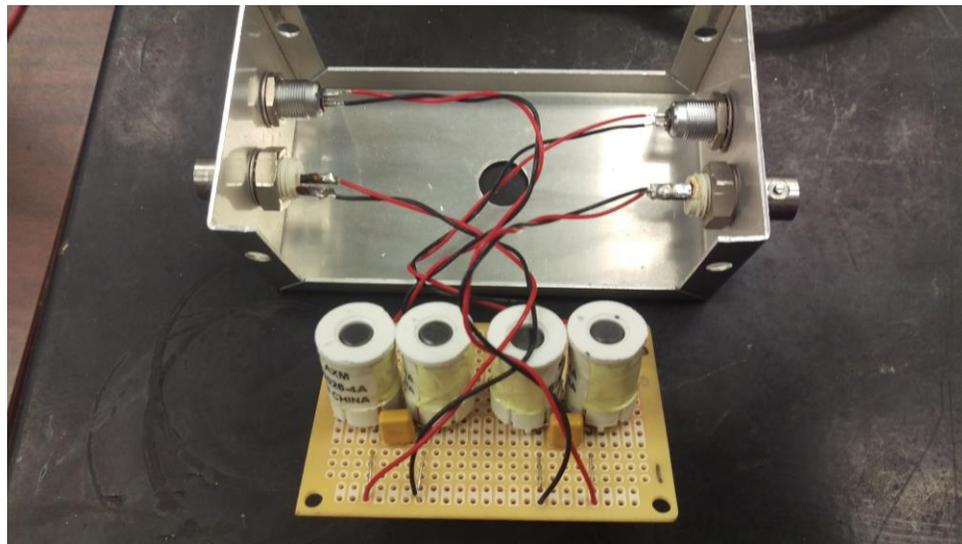

Figure 4.16 DC Noise Filter
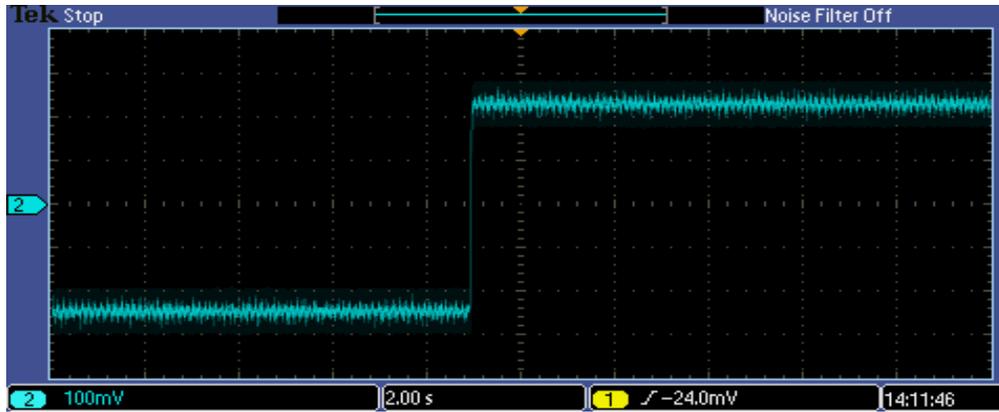
Figure 4.17: Corrected DC Noise

From Figure 4.17, we see a drastic reduction in the size of the noise relative to the signal (and overall). Note the change in scale from 200mV-100mV per box. Empirically, this results in a significant noise drop, shown in Figure 4.16 across a 50Ohm resistor. This allowed us a much more trustworthy data acquisition setup, particularly given the very low signal sizes required for this experiment. Resistance on the order of 10 Ohms maximum and currents pushing into the nA ranges required extremely precise voltage measurements accurate to the nV scale.

We have some preliminary resistance vs temperature (at various currents) curves that show some promising results. One thing that this experiment requires is an estimation and improvement of how low in current we can go while still making sense of the data. I've improved our measurement system in a few ways, and determined a lovely relationship between safe currents and the resistance of the sample we're attempting to measure. This was found using data shown in Figure 4.18 and 4.19. Considered differently, a way to estimate our uncertainty at a given measurement of resistance and current for signal size: $I_{safe} = 1.7279 * 10^{-7} e^{(-R/7.07011)}$

45
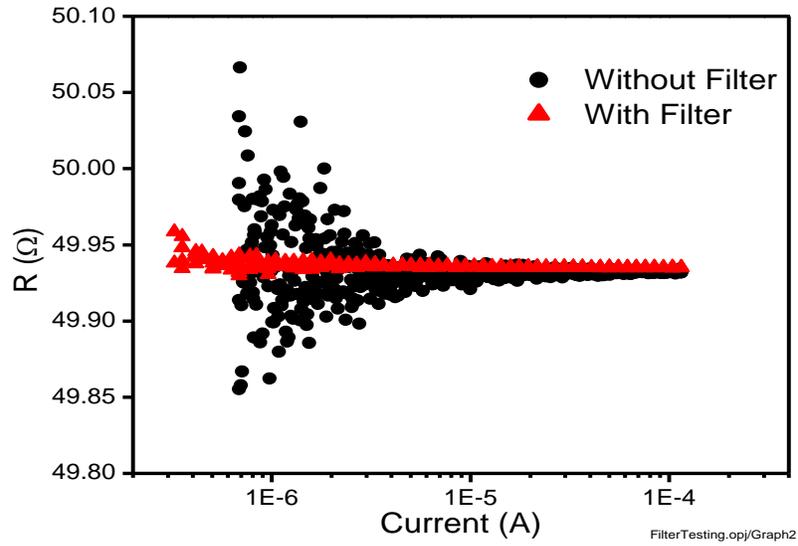
Figure 4.18: Low current extension comparison
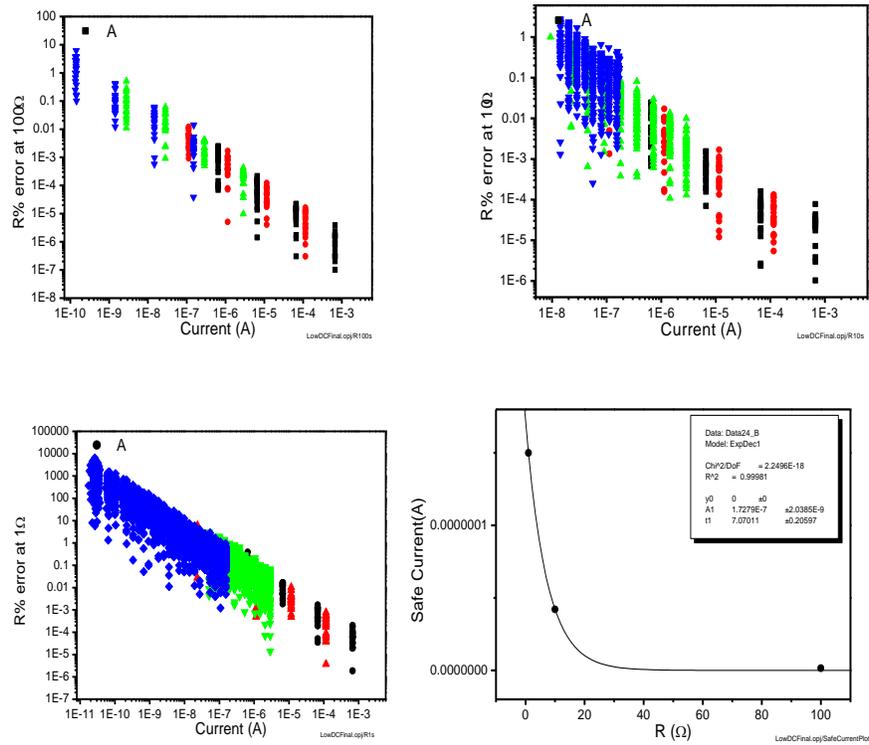
Figure 4.19: Error percentages vs Current for various resistors

4.2.5 PULSED QUASI DC

Our group uses a pulsed current setup that allows us to get to current densities higher than many other groups in our field. Measurements involving high current densities—which in the present case enter the current-induced depairing regime—cause both bulk dissipation (because the system becomes resistive) and heat generation at contacts. Both forms of these heating can be reduced by a using a short-duration, low-duty pulsed signals instead of the continuous signals, while continuing to maintain a conventional four-probe configuration to exclude contact resistances and thermal offsets. A Hewlett Packard HP 8015A Pulse Generator was used produce pulses of the desired shape and repetition frequency. A 50 Ohm cable carried the signal from the Pulse Generator the signal to the sample, and was terminated in a matching 50 Ohms impedance to avoid reflections. Since the sample's resistance (being in the superconducting state) was essentially zero over the experimental range of interest, the current through the circuit was set by the output voltage of the pulse generator and did not vary with field or temperature (i.e., the sample did not influence the current very much). The current as a function of time

$I(t)$ could be obtained by measuring the voltage across a series resistor or inductor. Both $I(t)$ and the voltage across the sample $V(t)$ were displayed on a Lecroy Waverunner 204 Xi, 2 GHz Digital Storage Oscilloscope. The single-shot sampling rate of 10 Gs/sec was used and 2000 pulses were averaged to yield low-noise data. Rise time in V(t) and I(t) is around 50 *ns* (from 10 and 90 % of top). The system was tested and calibrated by mounting various known standard resistors in place of the sample. As an example, Figure 4.20 shows $V(t)$ and $I(t)*R$ for a 14 *m*Ω test resistor.

47
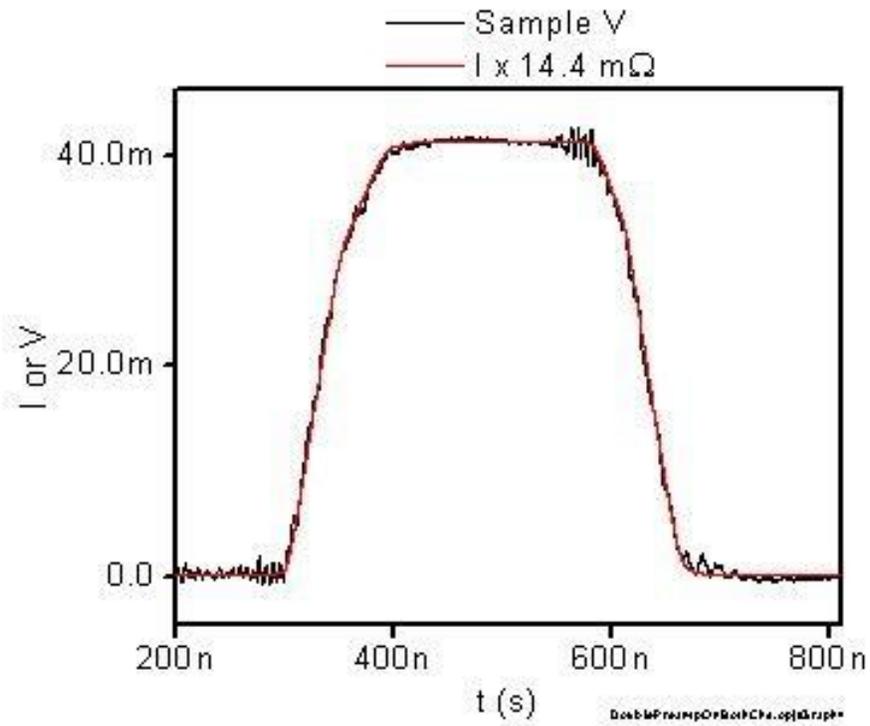
Figure 4.20: Oscilloscope Wave Forms for V (t) and scaled current I(t)R in pulsed current mode
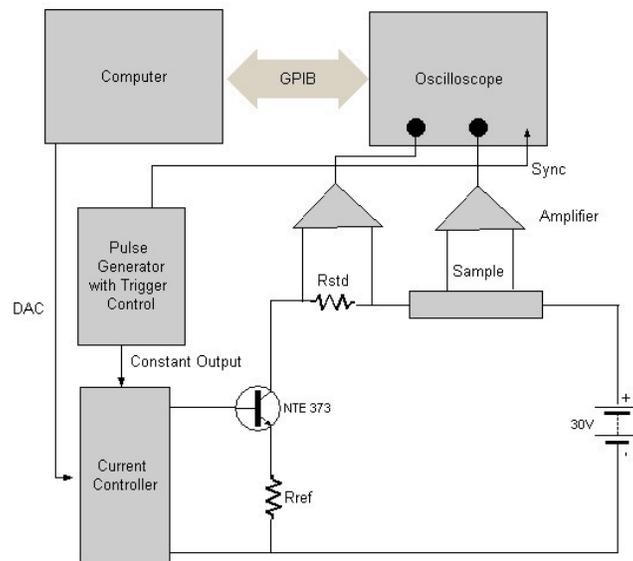

Figure 4.21: Four Probe Pulsed measurement circuit

CHAPTER 5:
RESULTS AND ANALYSIS

5.1 GENERAL MEASUREMENTS

5.1.1 CRITICAL TEMPERATURE

First and foremost, we needed to get an accurate measurement of the critical temperature. Here in figure 5.1 we see the resistance-temperature behavior of our two BT/FT samples at a low enough current (~13uA) such that there is insignificant shift in T_c due to depairing. We see that both bridges match well, implying a relatively homogenous crystal structure across the entire wafer.

We define our critical temperature to be at the onset of the superconducting state. Assuming the behavior of the "normal" state resistance would continue as the temperature drops, we extrapolate the curve out. Doing the same with the superconducting transition, we find the point which the two extrapolations meet and determine that to be the critical temperature. Shown in Figure 5.1, there is remarkable agreement between the two samples. As delicate as this material is, it shows great care was put into the lithography process. Due to them being measured separately, this is also great evidence in showing the long term stability of the measurement system. Pertaining to thermal cycling and the like, we see great agreement over the entire set of experiments which spanned several months.
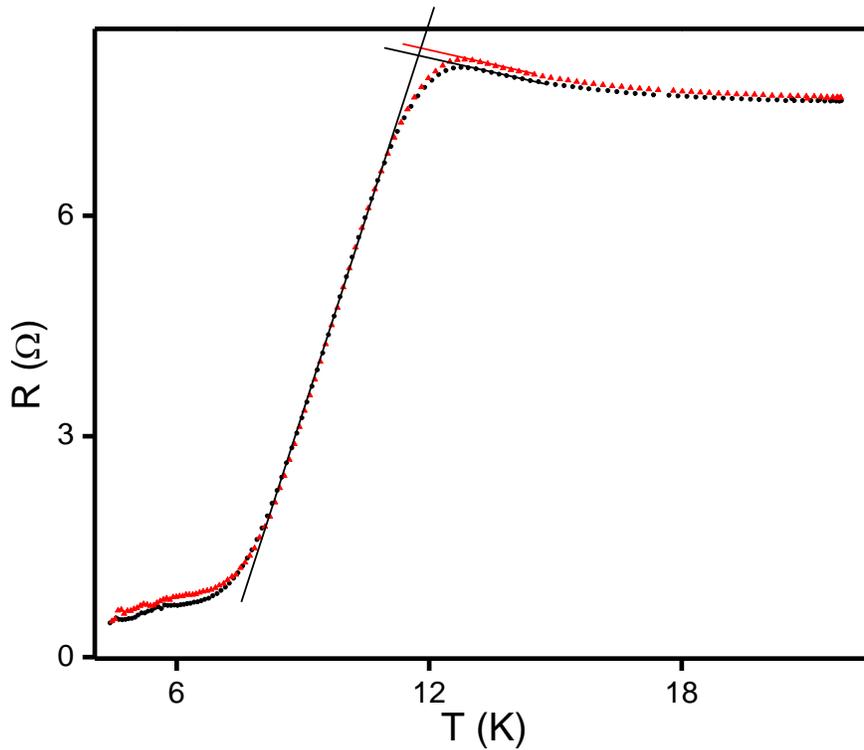
Figure 5.1 Resistance vs Temperature showing the SC state transition for the two samples used.

5.1.2 CRITICAL MAGNETIC FIELD (B_{C2})

The upper critical field was also measured for the BTFT system. We did this by measuring the resistance-temperature relationship at various applied B field in both parallel and perpendicular orientations. We then take constant resistance "cuts" to determine the relationship between the applied magnetic field and the temperature at which that field pushes the sample to various percentages of R_n. Figures 5.2 through 5.5 show this process step by step. First various Resistance Vs Temperature measurements were taken at various applied fields. Then we take these 'cuts' to determine and extrapolate RvsB for a very low T using WHH formalism.

50
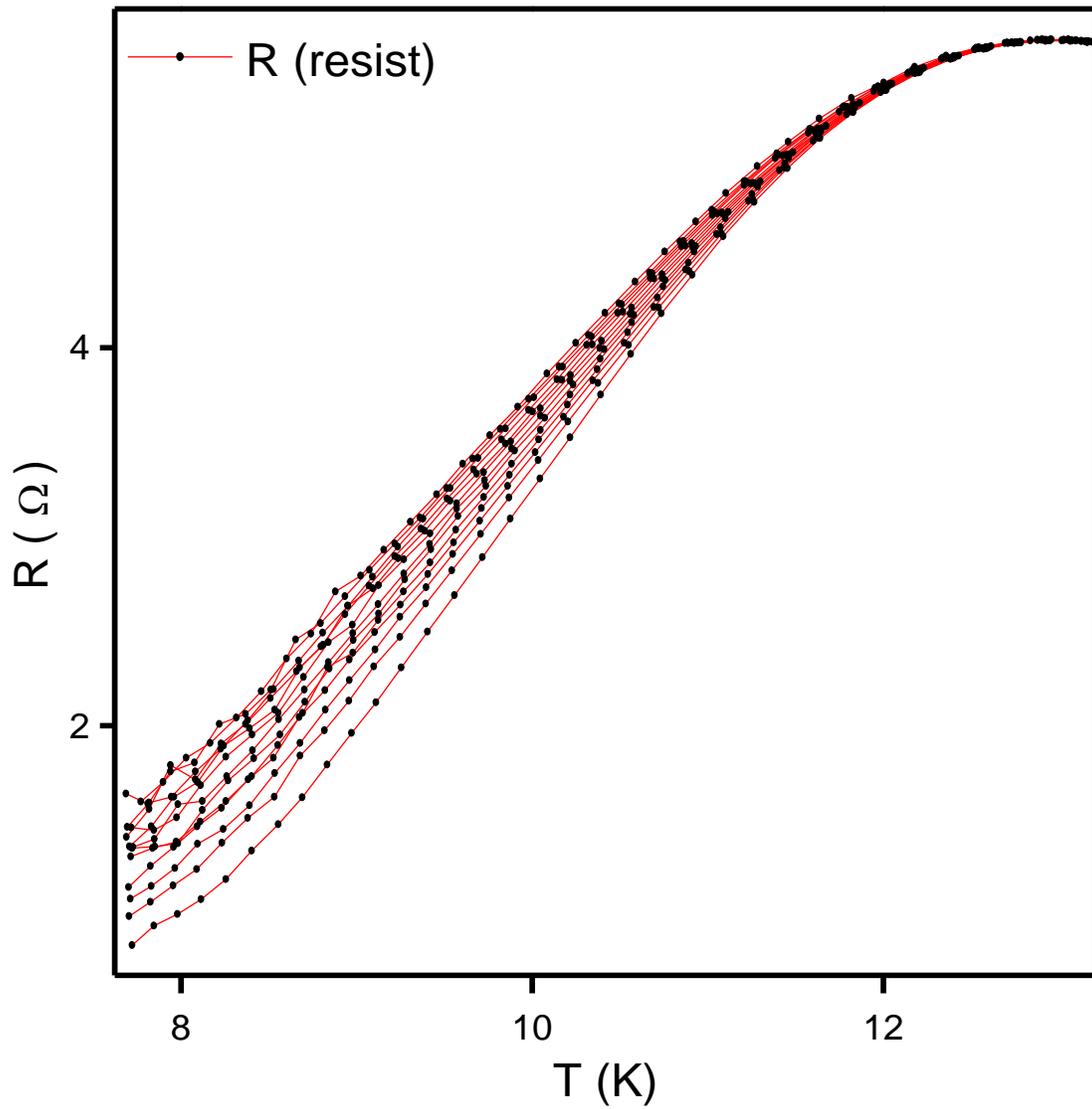
Figure 5.2 Resistance vs Temperature curves in a parallel field orientation from 0T-1.2T at 0.1T intervals
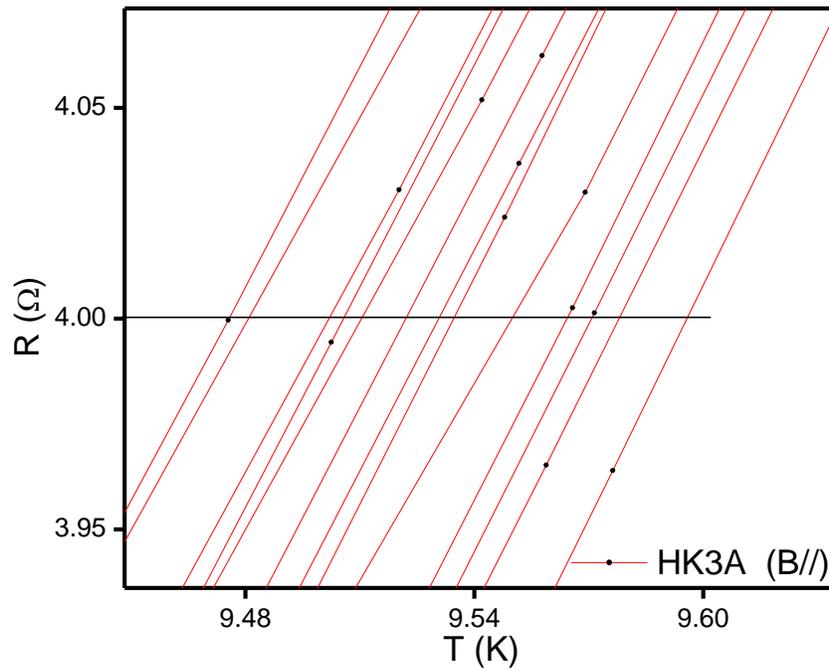
Figure 5.3 cut line for the R-T curves at 50%Rn
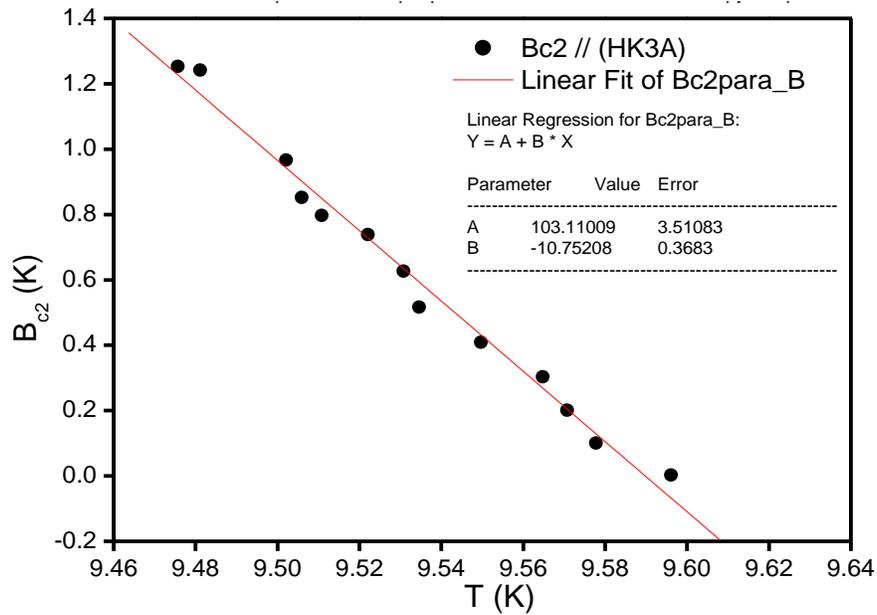
Figure 5.4 Parallel Bc2 vs Temperature, Bc2(0) found to be ~70T

52
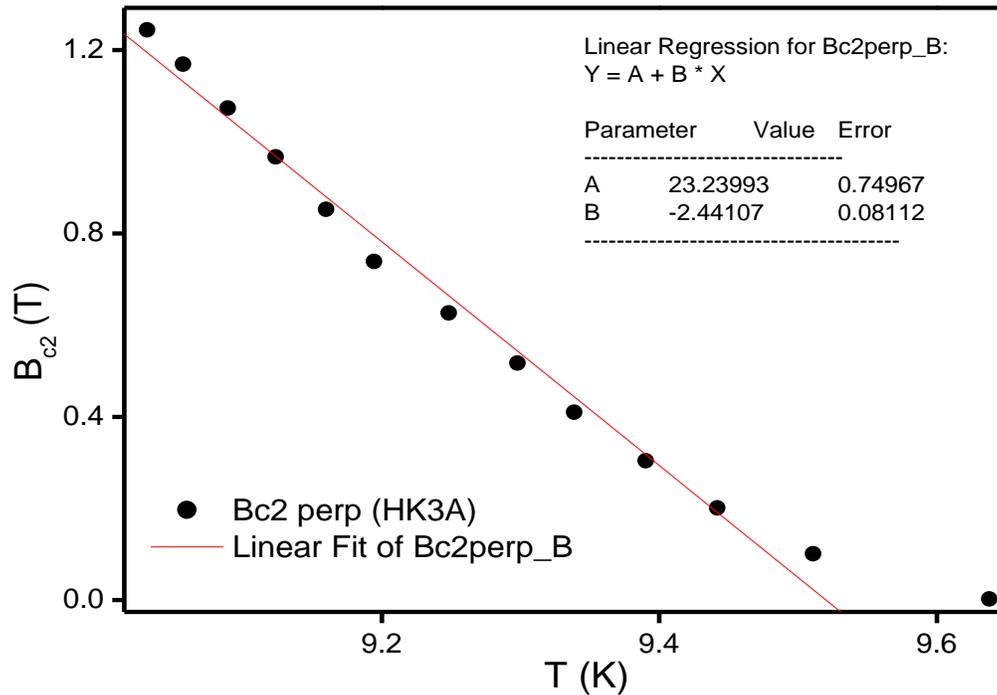
Figure 5.5 Perpendicular Bc2 vs Temperature, Bc2(0) found to be ~17T

5.2 DEPAIRING CURRENT DENSITY

The depairing current density or pair-breaking current is one of intrinsic

parameters that sets a fundamental limit to superconductivity survival. It is the current

density at which the kinetic energy of the superconducting carriers becomes equal to

the binding energy of the Cooper pairs. By increasing T, B and j, superconducting gap Δ

decreases. The boundary at T, B and j phase that Δ vanishes, separates superconducting

state from normal state and all these parameters attain their critical values T_c, B_{c2} and j_d

respectively. Any of these functions can separately define critical boundary.

T_c and B_{c2} measurements are done routinely while j_d is seldom measured due to

technical difficulties associated with sample heating at high currents [10]. A series of

useful reviews have been given on the calculation of the depairing current. These

53

theoretical calculations cover different regimes. The simple London equations are valid at T_c, but it failed at the lower temperature since it did not take into account the effect of the change in the order parameter with the current. The GL theory gives a good phenomenological treatment that works well close to T_c. For low temperatures, some other theories based on the microscopic theories were proposed. Here, j_d can be obtained in a simple London approach by equating the kinetic energy and condensation energy density expressions:

$$\frac{1}{2}n_s m^* v_s^2 = \frac{\mathbf{B}_c^2}{2\mu_0} \tag{46}$$

In this derivation, it is assumed that n_s is not affected by j when it gets closer to j_d. This formula seems to be far from reality, because it does not consider the fact that density of electrons is changing. But gives us an idea that j_d depends on both critical field and the penetration depth. Then, the velocity of the quasiparticle in a superconductor can be obtained by:

$$_s = \frac{\hbar}{m^*}\left(\nabla\varphi - \frac{2\pi}{\Phi_0}\mathbf{A}\right) \tag{47}$$

If we substitute above equation in (Eq. 36) and put the derivative of that equal to zero, we can find maximum value for v_s and J_s that beyond that there will not be any ψ that minimizes the free energy.

$$a + b\psi_0^2 + \frac{1}{2}m^* v_s^2 = 0 \tag{48}$$

The optimum of ψ_0 that minimizes free energy at fixed v_s is

$$\psi_0^2 = \frac{|a|}{b}(1 - \frac{m^*v_s^2}{2|a|}) = |\psi_m|^2[1 - (\frac{\xi m^*v_s}{\hbar})^2] \tag{49}$$

By putting above equation in into Eq. 48, we get to corresponding supercurrent density,

$$j = 2e|\psi_m|^2[1 - (\frac{\xi m^*v_s}{\hbar})^2]v_s \tag{50}$$

For calculating maximum current we put $\frac{\partial j}{\partial v_s} = 0$ and $v_s = \hbar/\sqrt{3}m^*\xi$ we get .

This current now can be identified as maximum possible value for current which is the

depairing current:

$$j_d = \frac{4e|\psi_m|^2\hbar}{3\sqrt{3}m^*\xi} \tag{481}$$
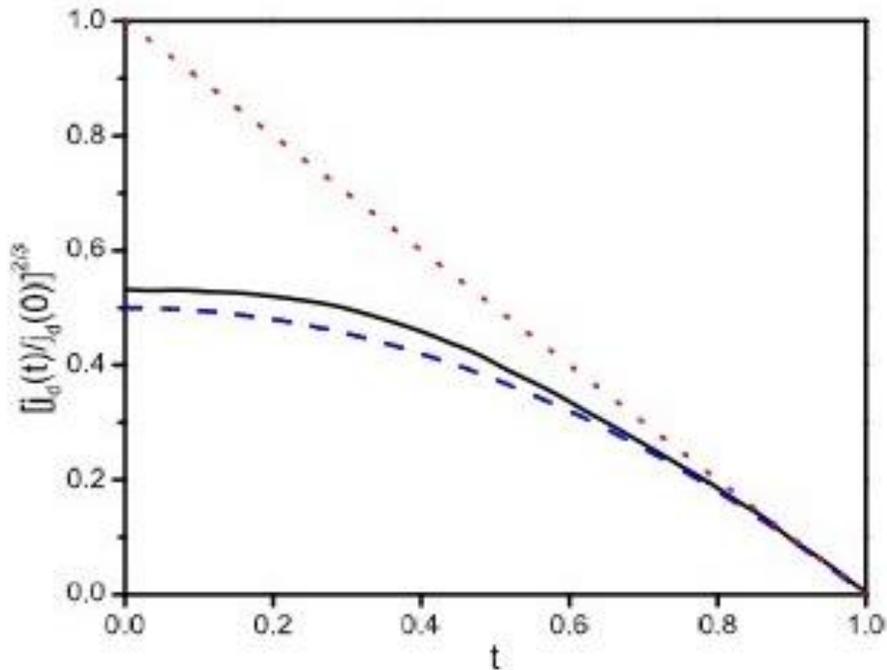

Figure 5.6 Temperature dependence of jd from different theories.
Replotted from Ref [17]. The solid curve is KL theory, the dashed one is Eq. 55 and the
dot one is GL's result.

55

If we combine the previous equation with London penetration depth equation (Eq 46), we eventually get

$$j_d = \frac{\hbar}{3\sqrt{3}\mu_0 e\lambda_L^2 \xi} = \frac{\Phi_0}{3\sqrt{3}\pi\mu_0\lambda_L^2(T)\xi(T)} \tag{52}$$

By considering $t = T/T_c$, $\lambda_L(t) = \lambda_L(0)/\sqrt{1 - (t)^4}$ and $\xi(t) = \xi(0)/\sqrt{1 - t}$ for temperatures close to T_c, shift in T_c defined at a given B and j as a function of applied current can be calculated:

$$1 - \frac{T_c(j)}{T_c(0)} \approx \left(\frac{1}{4}\right)^{\frac{2}{3}} \left[\frac{j}{j_d(0)}\right]^{\frac{2}{3}} \tag{493}$$

In this equation we can see the proportionality to $j^{2/3}$. $j_d(0)$ is then equal to:

$$j_d(0) = \sqrt{\frac{2\Phi_0}{27\pi\mu_0^2}} \left(\frac{\sqrt{\mathbf{B}_{c2}(0)}}{\lambda_L^2(0)}\right) \tag{54}$$

here $\mathbf{B}_{c2}(0) = \Phi_0/2\pi\xi(0)^2$ is upper critical field at zero temperature. In the *MKSA* system, it becomes:

$$j_d(0) = 5.56 * 10^{-3} \rho \frac{B_{c2}(0)}{\lambda^2(0)} \tag{55}$$

Here j_d is in A/m^2, $\mathbf{B}_{c2}$ is in Teslas and λ is in meters. In above equation, we took off the subscript of λ_L only to prevent confusion. Joule heating will give an apparent shift $\Delta T_c \propto \rho j^2$ if for any reason heat removal from the sample is ineffective. Different groups have done calculations for pair breaking current. Kuprianov and Lukichev among them had closer results to phenomenological expression. Phenomenological j_d was calculated, by inserting temperature dependence of B_c and λ

$$j_d = \frac{j_d(0)}{2\sqrt{2}}(1 - t^2)^{3/2} \tag{56}$$

56

It is important to point out that the predictions on the temperature dependence of j_d from these theories are the same when the temperature is near T_c. In Fig.7, the results of different theories are compared.

In the limit of lower temperature and in the presence of a uniform velocity v_s the quasiparticle energies shift by $-hk_F v_s$ where k_F is the wavevector at the Fermi surface. In superconducting state, n_s stays roughly constant to the point v_s is reaching its critical value v_d. At that point the shift in energy will be equal to the energy gap and the velocity gets to $v_o = 2h/m^*\xi$ which is the maximum velocity of quasiparticles in GL's framework [14].

$$v_d = \frac{\Delta}{\hbar k_F} = \frac{2\hbar}{m^*\xi} \tag{50}$$

Here m is the mass of one electron and ξ is the coherence length. j is proportional to v_s until it gets to v_d where value of n_s is dropping. For the limit $v_s \ll v_\Delta$, all electrons contribute to supercurrent $j_s = 2en_s v_s$. For temperatures close to T_c, the density of quasi particles is proportional to the order parameter $|\psi|^2$ in GL frame, but at low temperatures a more microscopic calculation is required to take into account the effect of the modification on the quasiparticle density by the drifting velocity. The maximum that current can get is slightly higher than the value at v_d. By a good approximation it can be said that $j_d ' e^* n^*_s v_d$ and therefore:

$$j_d \simeq \frac{m^* c^2 \Delta}{4\pi e^* \lambda^2 \hbar k_F} \simeq \frac{c^2 \hbar}{2\pi^2 e^* \lambda^2 \xi} \tag{58}$$

57

Magnitude of ξ can be calculated by knowing the value of B_{c2}. Here k_F is a constant number and Δ has temperature dependence. From the *RHS* of above equation the temperature dependence of j_d is calculated

$$j_d(T) = j_d(0)\left(\frac{\lambda^2(0)}{\Delta(0)}\right)\frac{\Delta(T)}{\lambda^2(T)} \tag{59}$$

By using the *RHS* of magnitude of $j_0(d)$ in *BCS* frame and in *MKSA* system is estimated to be

$$j_d(0) = 9.2 * 10^{-3}\,\rho\,\frac{B_{c2}(0)}{\lambda^2(0)} \tag{60}$$
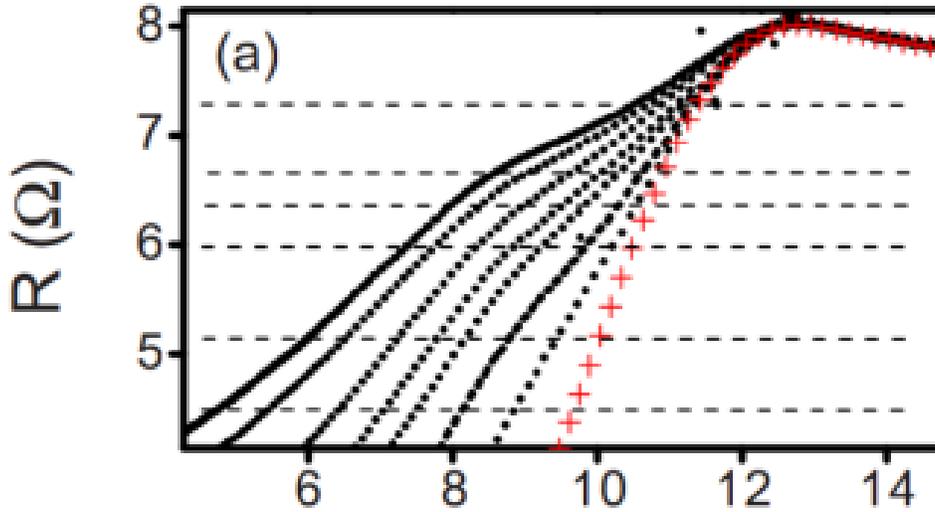
*Figure 5.7 Resistance vs temperature for various applied currents*

Figure 5.7 shows resistive transitions in B =0 at various applied currents. Taking various resistance "cuts" R_c, as shown by the horizontal dashed lines, one can define the temperature that corresponds to a particular "resistive critical current" as the value where the curve for that particular applied current intersects the respective horizontal line. (As

will be discussed later in this section, as T is lowered below T_c, the normal-state

conductance is nearly temperature independent and dominated by the normal

conductance of the interface layer itself; the parallel conductance of the FeTe layer,

which has a negative R(T) slope, provides a diminishing contribution below Tc.) Plotting

these currents and temperatures for each criterion, as $I^{2/3}$ versus T and simply I versus T,

results in Figs. 5.7 and 5.8, respectively.
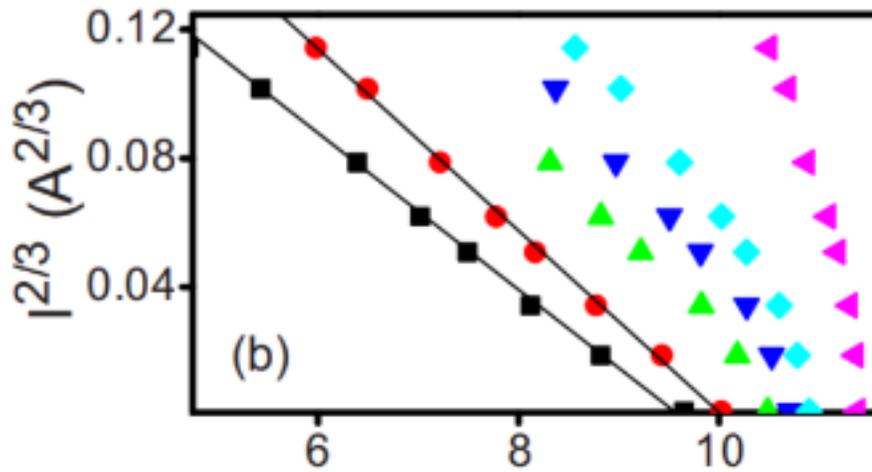
Figure 5.8 Current^2/3 vs Temperature at various Rc
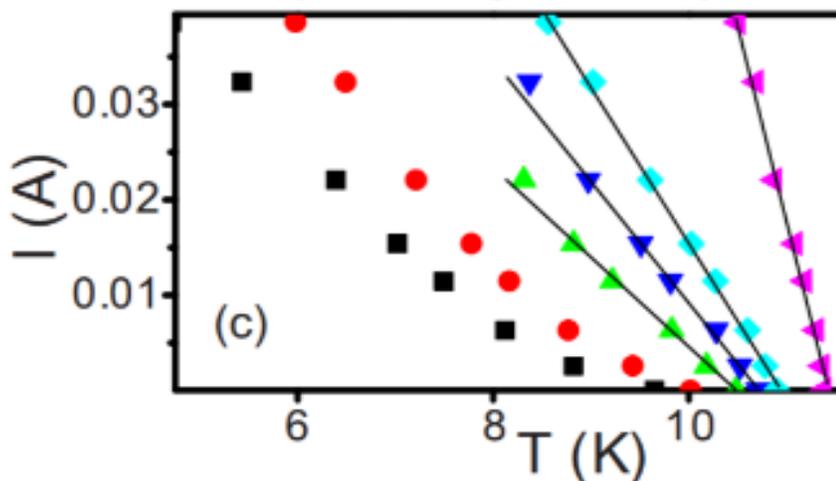
Figure 5.9 Current(I) vs Temperature at various Rc

As can be seen, there is a threshold around T ≈10 K below which the data follow the classic I2/3 ∝ T behavior expected for the temperature dependence of the depairing current [Fig. 5.9 (a)]; above 10 K, a linear I ∝ T behavior is followed [Fig. 24]. Figure 25 shows a similar set of plots for sample B; the threshold temperature is seen to be around 10.2 K. This cross over in the power law occurs at a temperature that appears to be close to the T_{BKT} found by He et al. (Qing Lin He, 2014). There are several possibilities for this cross over.
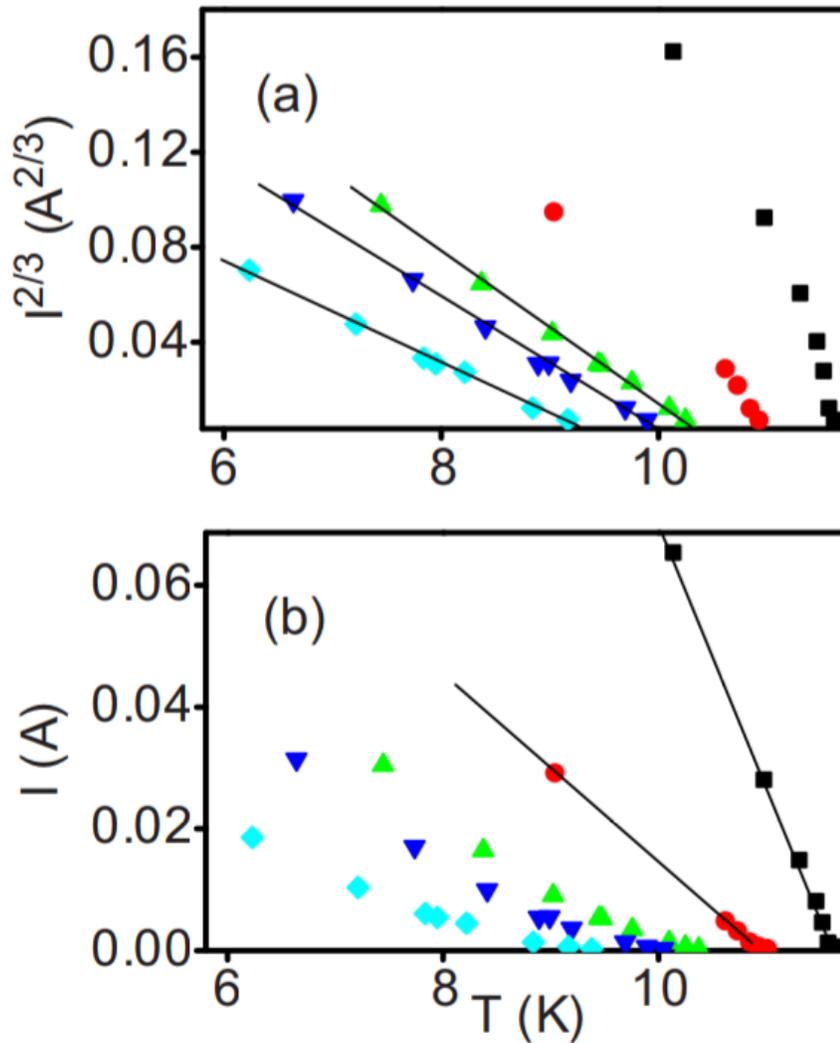
Fig 5.10 Currents vs Temperature for Sample B

With increasing current, resistance appears in a superconductor at zero external magnetic field chiefly through the two processes of pair breaking and flux flow associated with the perpendicular component of the self-field of the applied current. The self-field has the profile $B\perp self(x)=[\mu_0 I/2\pi w]\ln[(w+2x)/(w-2x)]$ across the width of the bridge (origin taken at the center of the bridge), with the logarithmic divergence cut off by the film thickness to $B\perp self(\pm w/2)=(\mu_0 I/2\pi w)\ln(w/d)$.

Even this edge field is only ∼10 mT, which is dwarfed by B_{c2} and even exceeded by the lower critical field B_{c1} over most of the temperature range, so that pair breaking dominates over flux dissipation. However, the opposite is true closer to T_c where the self-field of the fixed current I will exceed B_{c1} and will lead to appreciable flux dissipation due to the penetration of vortices and anti-vortices at the opposite edges of the film and their subsequent annihilation in the middle of the strip. Since $B\perp self \propto I$, we expect, as observed experimentally, a linear dependence of the threshold I on T because of the linear temperature dependencies of $B_{c2}(T)$ and $B_{c1}(T)$ near T_c and the flux-flow formula $\rho \approx \rho_n * B/B_{c2} \propto I*/B_{c2}(1-T/T_c)$ leading to $I* \propto - T$ for a fixed ρ, where $B_{c2} = dB_{c2}/dT$ at $T = T_c$. As T is increased beyond T_{BKT}, the plasma of dissociated Vortex-antiVortex pairs that appears above T_{BKT} leads to a suppression in the order parameter and a consequent boost in the flux-flow resistivity. This may explain why the cross over between pair-breaking and self-flux-dissipation regimes appears to be tied to the BKT temperature.

The condition that the self-field at the edges exceeds $B_{c2}(T)$ gives currents well above the values observed in our experiments, so we suggest the following scenario of the crossover based on the penetration of vortex semi-loops at the film edges. A rough estimate of the current level required to promote penetration of a vortex at the film edge

can be obtained from the energy balance between the work of the Lorentz force I0d/2w to form a vortex semi-loop of diameter equal to the film thickness d at the edge [11], and the self-energy of the vortex $2d/4\pi\mu_0\lambda2$ at the film edge [12]. The condition I0d/2w 2d/4$\pi\mu_0\lambda$2 then yields $I = I_0(1-T/T_c)$. Here, I0 w0/2$\mu_0\lambda_2$(0) ≈0.2 A for λ(0)=124nm estimated below from our experimental data. Another window on current induced depairing is provided by high pulsed current-voltage characteristics at various fixed temperatures. As shown in Figure 25, the current is able to drive the system completely normal at all temperatures. This provides one of the cleanest methods [13] for measuring the temperature dependence of the normal-state resistance Rn(T) below the transition. From Figure 5.10, it is seen that Rn is approximately the same for the different temperatures. This is typical of metallic systems in which Rn tends to approach a constant residual value as T →0; however, our measurement is sensitive enough to detect small variations in Rn (T), which will be plotted and discussed later. The transition in R(I) becomes rounded as T → Tc and naturally becomes flat and Ohmic for T > T c. Here, we will define the "resistive critical current" I∗ at a criterion of 90% of the Rn plateau, anticipating that I∗ ∼ Id as T →0, because this limit represents the current required to drive completely normal a fully condensed state.

However, the most important addition of this research is the added second order effect where there is also a "depairing" region where vortex and antiVortex pairs are pulled apart. This is a new phenomenon and does not have significant overlap with the depairing discussed here. At our values of the depairing current density near the transition, we are several orders of magnitude away from the V-aV and BKT regions.
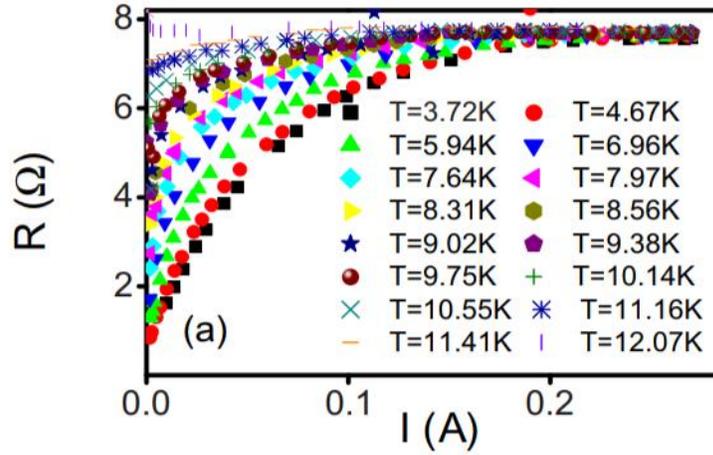
Figure 5.11 Resistance Vs Current, various Temperatures, Near top of transition
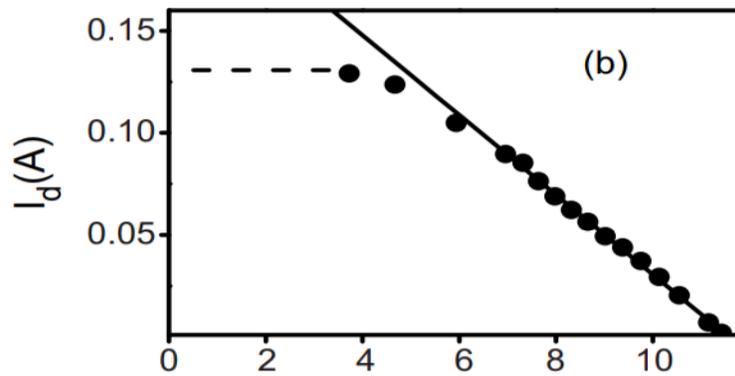

*Figure 5.12 Depairing Current Vs Temperature Sample A*
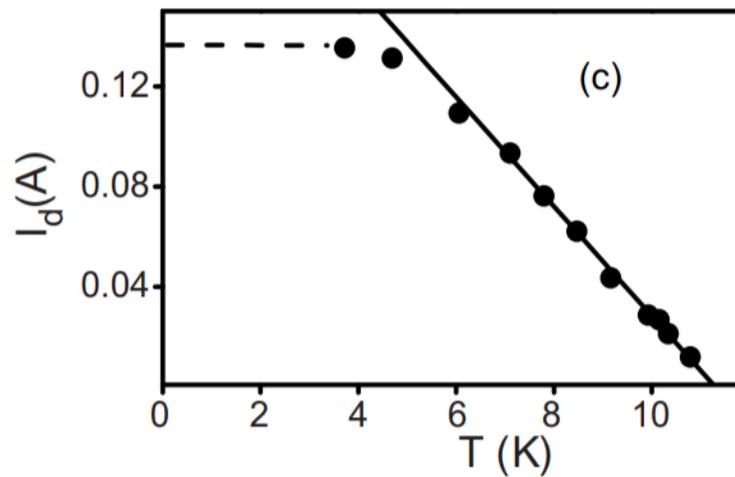
Figure 5.13 Depairing Current Vs Temperature Sample B

Figures 5.9 and 5.10 show these measured $I*(T)$ functions for samples A and B, respectively. The observed intercepts of the linear portions, $I_0 = 0.23$ and 0.25 A are consistent with the rough estimate of $I_0 \approx 0.2$ calculated earlier. The dashed horizontal lines in panels (b) and (c) provide the values $I_d (T \rightarrow 0)$ 0.131 and 0.136 A. In order to obtain, more accurately, the intrinsic ρ_n and depairing current density Jd of the 7-nm-thick superconducting interfacial layer itself, we need to subtract the small parallel current through the underlying FeTe.

A separate measurement of pure FeTe deposited on ZnSe/GaAs, without the Bi_2Te_3 top layer, reveals the resistivity curve plotted in Fig. 4(a), which has an order of magnitude (~ 100 μm) that is characteristic of many of high-temperature superconductors. The corrected j_d (T $=0$) then works out to be 1.5×108 A/cm^2 for both samples, which is a typical value (jd ranges/ 107–109 A/cm^2 for most superconductors). Similarly, the Rn plateaus of Fig. 5.12 were corrected using the Fig. 5.13 (a) function, which leads to the intrinsic $\rho_n(T)$ for the two samples shown in Fig. 513(b).

This absolute value of ρ_n (T $\rightarrow 0$) ~ 200 ncm represents an extraordinarily conductive normal state for a superconducting system. This information will be analyzed below to see what can be learned about the scattering rates, after obtaining information on the superfluid density and carrier concentration from j_d. Before using the results shown above to extract intrinsic microscopic characteristics of the Bi_2Te_3/FeTe interfacial superconductor, we note that the combination of Bi_2Te_3 and FeTe band structures are likely to lead to multiple bands intersecting the Fermi level. As a result, extracting electronic parameters from experimental data generally requires formulas for j_d, H_{c2}, and λ obtained for multiband superconductors [14,15].

64

However, using these formulas greatly increases the number of microscopic input parameters, which are currently not known. In addition to electronic parameters in different bands, these include at least four matrix elements of superconducting pairing constants, as well as other parameters that quantify the symmetry of the order parameter and details of microscopic pairing mechanism. To avoid these complications and to get a qualitative insight into the electronic parameters of BT/FT, we use a universal anisotropic Ginzburg-Landau (GL) theory, assuming only one dominant band. The values computed with these assumptions turn out to be self-consistent, thus providing some justification for this approach. We first use the anisotropic GL theory to extract the coherence lengths $\xi(T)$ and $\xi_\perp(T)$, parallel and perpendicular to the interface, respectively. Now we have a perpendicular-to-interface $B_{\perp c2}(0) = 0/2\pi\xi_2(0) \approx 17$ T and a parallel-to-interface $B_{c2}(0) = 0/2\pi\xi(0)\xi_\perp(0) \approx 40$T, leading to an in-plane $\xi(0) \approx 4.4$ nm and a perpendicular $\xi_\perp(0) \approx 1.9$ nm. Note that in an interface superconductor of thickness d, the formula $B_{c2} = 0/2\pi\xi\xi_\perp$ is applicable if $\xi_\perp(T) < d$, whereas near Tc where $\xi_\perp(T) > d$, we have $B_{c2} = 0/2\pi\xi d$. Our measured in-plane $j_d(0)$ can be related to the in-plane $\lambda(0)$ and the perpendicular $B_{\perp c2}(0)$ through [8] $j_d = (1/\mu_0\lambda_2)(20B_{c2}/27\pi)^{1/2}$, which gives $\lambda(0) = 124$ nm. The corresponding zero-T Pearl screening length is $(0) = 2\lambda_2/d = 4.4$ μm.

As emphasized in our earlier work [5,17], the combination of Bc2 and jd provides a useful method for obtaining a single-band λ purely from transport measurements, which directly gives an absolute value of $\lambda(0)$ and is unaffected by magnetism in the material. We now utilize the information obtained about λ and ρ_n to estimate the carrier concentration, Fermi surface parameters, and mean free path characterizing the normal state of the interface layer, using the effective single-band approximation mentioned

65

above. From $\lambda_2(0) = m*/\mu_0 n_s(0)e^2 \approx m/\mu_0 ne^2$, applicable in the clean limit at T = 0, we get

n $\approx 1.8 \times 10^{21}$ per cm^3, assuming that the effective electron mass m* equals the free

electron mass, m, e is the electron charge, and the carrier concentration n equals the

superfluid density ns.

In a two-band superconductor, the penetration depth would depend on intraband

densities and effective masses, according to $\lambda^{-2} = e^2\mu_0(n_1/m_1 + n_2/m_2)$, where the indices

1 and 2 correspond to the respective bands [15]. The effective single-band value of n

evaluated above is similar to n characteristic of high-temperature superconductors and

about two orders of magnitude lower than n in highly conductive metals such as copper.

This low value of n together with the very high normal conductivity implies a rather long

scattering time τ and mean free path l. The Fermi wave number for this n computes to

$k_F(3D) = m*v_F/ = (3\pi^2 n)^{1/3} = 3.8 \times 10^9$ m^{-1} and $k_F(2D) = (2\pi nd)^{1/2} = 9.0 \times 10^9$ m^{-1} in three

and two dimensions, respectively. In both cases, the Fermi wavelength $\lambda_F = 2\pi/k_F d$,

validating the continuum approximation for states along the perpendicular direction and

justifying the anisotropic 3D treatment of the normal state. Then from the Drude

relationship $\rho \approx m/ne^2\tau$, we then get $\tau \approx 10$ ps, which agrees well with the scattering rates

($\sim/0.05$ meV = 13 ps) measured by Pan et al. [18] using spin- and angle-resolved

photoemission spectroscopy. Combining this value of τ with the Fermi velocity v_F =

$k_F/m \approx 440$ km/s, we get l = $v_F\tau$ = 4.2μm. The very long l, which well exceeds d, indicates

that scattering from the faces that bound the superconducting layer is of a specular nature.
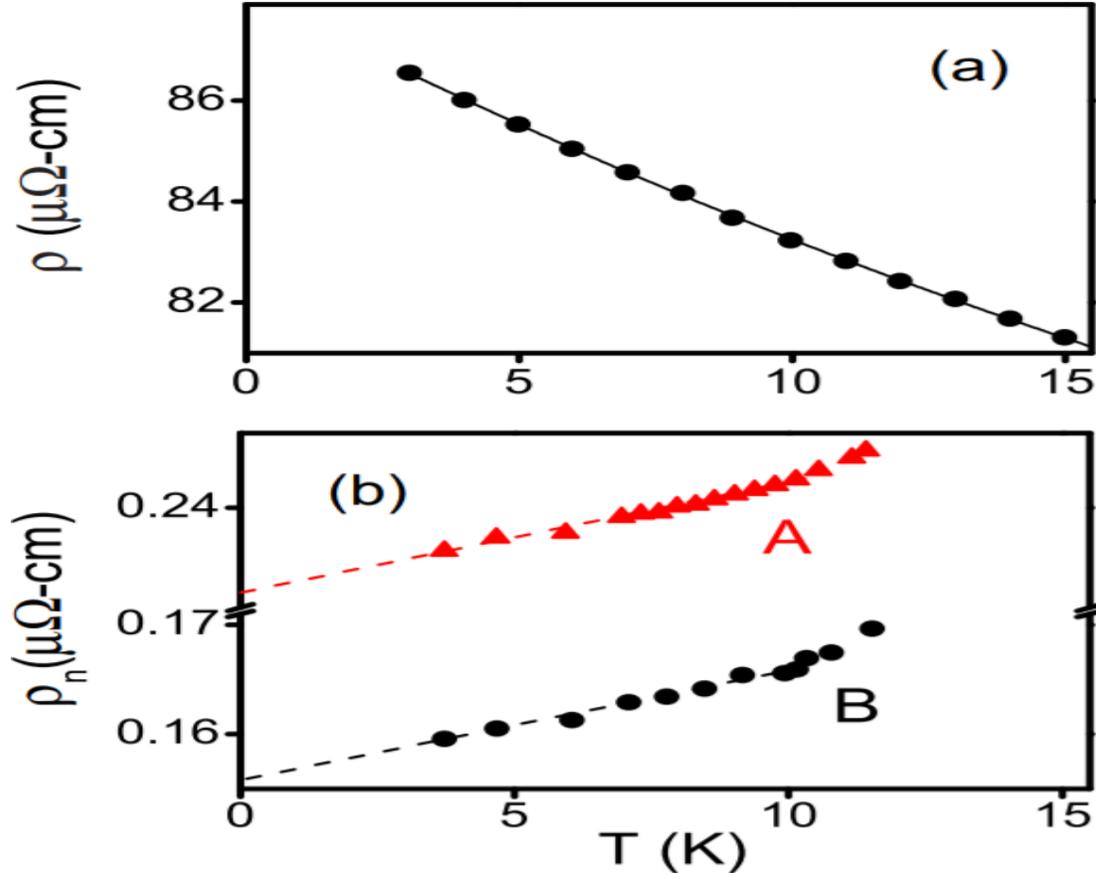
5.14 (a) Resistivity of pure FeTe with no BiTe layer.
(b) Intrinisic resistivity of the interface for two samples

5.3 V-aV DEPAIRING AND VORTEX EXPLOSION

Fig. 5.14 (a) shows the extended R(I) (resistance-current) response, with the lower portion measured using continuous dc currents and the higher portion measured using fast pulsed signals. The temperature for these data is T=10.5 K, which is above T_{BKT}. On the left of the graph, notice that the resistance plateaus to a finite value as $I \rightarrow 0$, indicative of an Ohmic response. This is expected because of the plasma of unbound vortices and anti-vortices that exists in thermal equilibrium above T_{BKT}, even in the absence of the driving force of a current. Fig. 5.14 shows similar curves at $T = 3.7$ K $\ll T_{BKT}$.
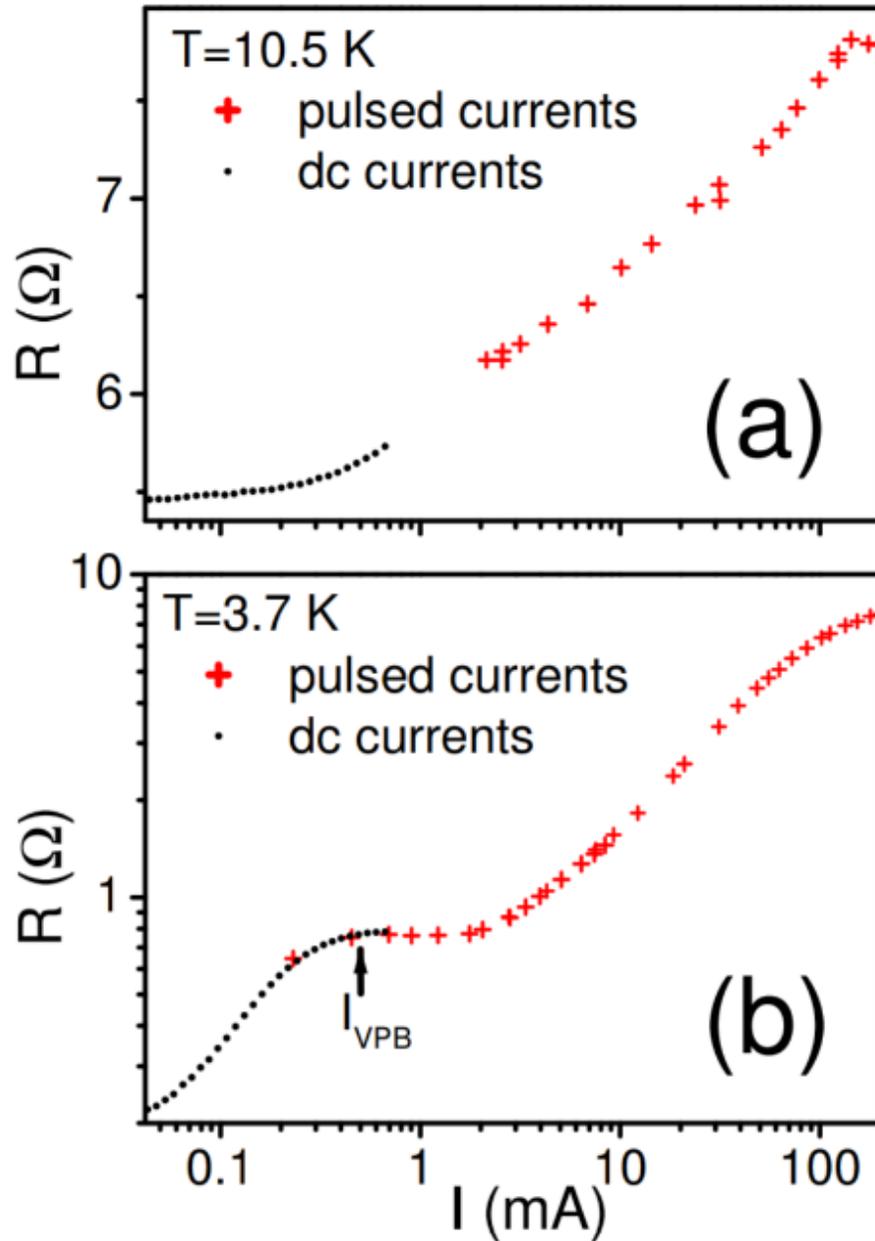
Figure 5.15 Above the lower BKT regime bound, the R does not tend toward zero. Below, there is a secondary current dependent transition

In this case R → 0 as I → 0, instead of reaching an Ohmic plateau, indicating that

the vortex-antivortex pairs become bound and non-dissipative as the separating force of

the current vanishes, since purely thermal dissociation vanishes for T <T_{BKT}. Tracing this

R(I) curve from lowest to highest I, the resistance rises with increasing I and momentarily

68

www.manaraa.com

saturates to a constant value in the middle of the graph above I & 0.5 mA. In anticipation that this plateau corresponds to the condition when most of the vortex-antivortex pair population has become unbound from the force of the current, we will call this quantity $I_{VPB} \approx 0.5$ mA, the "vortex-pair-breaking current". We can obtain a simple estimate of I_{VPB} in the following way. The inter-vortex potential is given by:

$$U = \frac{d}{2\pi\mu_0} \left(\frac{\Phi_0}{4\pi\lambda}\right)^2 \left(ln\frac{|\vec{r} - \vec{r}'|}{\xi} - ln\frac{w}{\xi}\right) \tag{51}$$

where λ is the magnetic penetration depth and $\Phi_0 = h/2e$ is the flux quantum. The current density exerts a constant force $j_d\Phi_0$ on the vortex, adding a potential $-j_d\Phi_0 r$ to the equation. Defining the dimensionless interaction u = Ud $\pi\mu_0$ Φ_0 $4\pi\lambda 2$, and the dimensionless length x = |r − r′|/ξ, and including a factor x/(x + ξ) as a cutoff of the vortex-antivortex interaction at distances of the order of the coherence length, we can express the interaction as:

$$u = \frac{1}{2}\frac{x}{(x + 1)}\left(ln\frac{x}{l}\right) - kx \tag{52}$$

For k = 0, this has a single minimum at x = 0.718 (i.e., for |r− r′| ξ), which represents the equilibrium separation of the paired vortices at zero current. For k > 0, the potential has a maximum for x > 1 outside the core and goes to −∞ beyond this peak. The vortices could dissociate by being thermally activated over or by tunneling through this peak. As the current (k) is increased, the peak becomes progressively reduced until it finally merges with the minimum. At this point the vortices are no longer bound, and this current can be interpreted as I_{VPB}.

A numerical calculation shows that this happens at k = 0.128. Taking λ = 124×10^{-9} m and ξ = 4.4×10^{-9}m [15],[22], this translates to a current density j = 6.28×109

69

A/m^2. For our sample dimensions of w = 11.6 µm and d = 7 nm, we get a current I_{VPB}=0.509 mA, in good agreement with the observed I_{VPB}≈0.5 mA. The model used here is similar to the one used by Kadin, Epstein, and Goldman [27] who investigated the transport response in quench condensed HeZe alloy films at lower current densities and temperatures in a closer range to T_{BKT}. Referring back to Fig. 1(b), upon further increase of the current beyond the plateau (I > 2 mA), there is once again a non-linear response as the current attains levels that are not only enough to dissociate the Vortex-antiVortex pairs but are high enough to break Cooper pairs. This is the regular (Cooper) pair-breaking (depairing) regime; here the depairing current I_d (∼0.1 A) signals entry into the normal state, upon which R(I) saturates to a constant (residual) value.

A detailed investigation of the upper depairing regime was conducted. Fig. 5.14 (a) and (b) show two extreme temperatures, one above T_{BKT} (with R→constant as I→0) and the other at the bottom temperature of the cryostat and well below T_{BKT} (with R→0 as I→0). To better demarcate the progression that differentiates these behaviors, we measured a complete set of dc R(I) curves at a sequence of temperatures shown in Fig 5.15. One observes two qualitative regimes: below some temperature T_v ∼ 6K, the curves are more closely bunched together and show a "fishtail" pattern with a convergence at I_{VPB} & 0.5 mA; whereas above T_v ∼ 6K, the curves are more widely separated and with decreasing T seem to stall around ∼ 6K before falling more rapidly. To better identify this cross over temperature T_v, a complete temperature-resistance curve was measured at a low value constant current (53 µA) corresponding to the left side of the graph in Fig. 5.17.
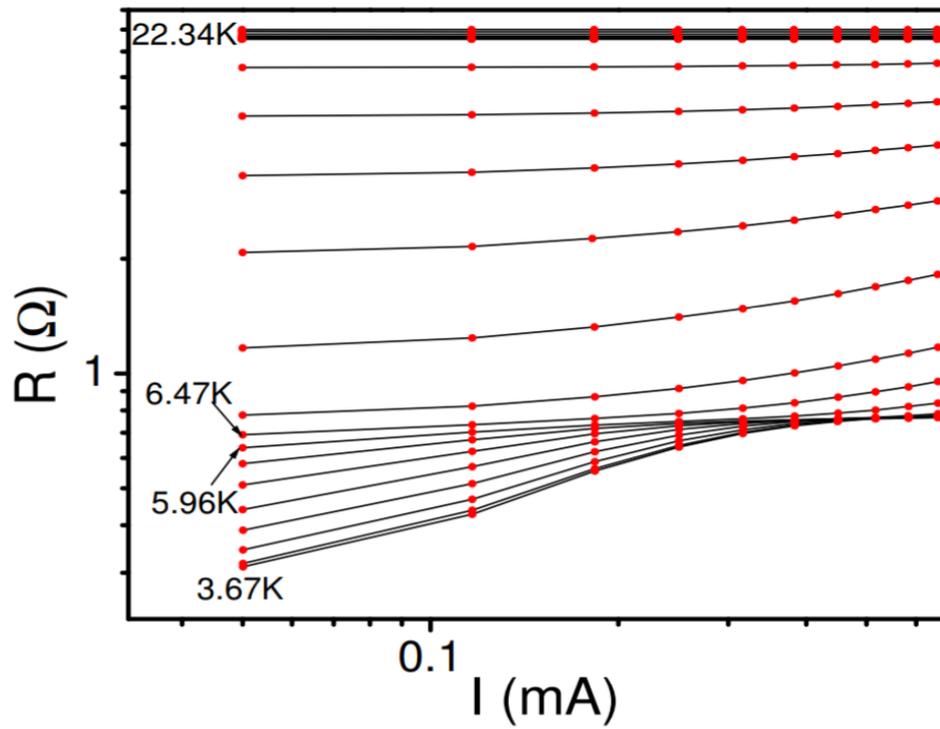
Figure 5.16 Set of Resistance vs DC current curves at various temperatures
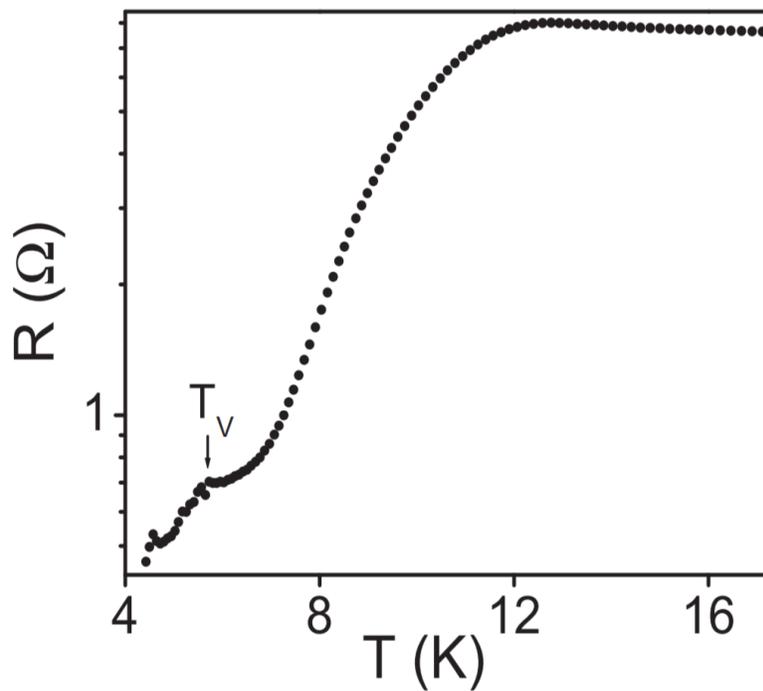

Figure 5.17 Resistance vs Temperature at low (~50uA) current

71

The result is shown in Fig. 5.16, which clearly shows a break below at Tv = 5.7 K, similar to what was previously observed in MoGe3. To qualitatively understand this observation, we first note that the conditions of temperature ($T \ll T_{BKT}$) and current ($I \ll I_{VPB}$) are such that the BKT mechanism will not provide appreciable dissipation (negligible population of unbound vortex-antivortex pairs). In this case the small amount of residual resistance will arise mainly through the GV process (unbinding of edge nucleated vortices from their antivortex images outside the edge).

The GV mechanism is facilitated by the Likharev exploded vortex condition [23], and thus the resistance is expected to decrease more rapidly below the vortex-explosion transition temperature Tv. To test the applicability of this Likharev vortex explosion phenomenon to the features observed here at Tv=5.7 K, we use the upper-critical-field measurements of He et al.5 to estimate the coherence length perpendicular to the plane: we have a perpendicular-to-interface $B_{\perp c2}(T=5.7 \text{ K}) = \Phi_0/2\pi\xi \approx 17$ T and a parallel-to interface $B_{c2}(T=5.7 \text{ K}) = \Phi_0/2\pi\xi_{\parallel}\xi_{\perp} \approx 27$ T, leading to a perpendicular $\xi_{\perp}(T=5.7 \text{ K}) \approx$ 1.78 nm. Multiplying this by 4.4 gives: $4.4\xi_{\perp}(T=5.7 \text{ K}) = 7.8$ nm which agrees well with 7 ± 1.1 nm thickness estimated by He et al.

Upon further investigation, we have proposed a new mechanism for this drop in resistance below the vortex explosion temperature. As, it would generally make more sense that, as more vortices would be allowed to exist below this temperature, this should result in more flux flow and therefore more resistance. However, we see a quick dip down to zero.

72
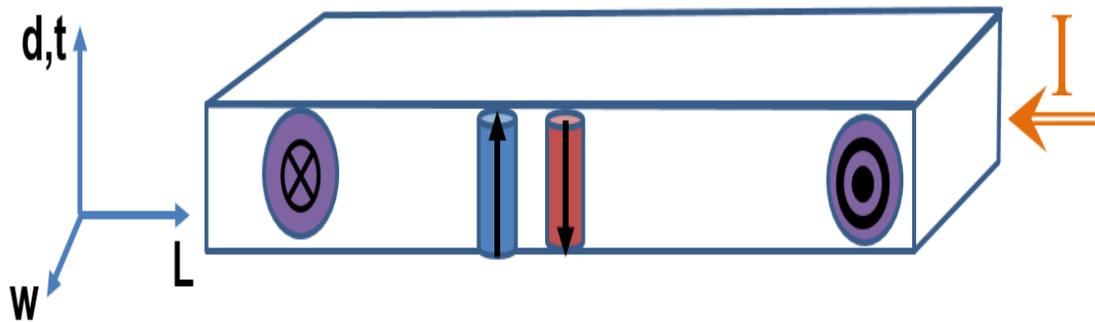
Figure 5.18 Showing allowed transverse vortices (purple) and Vortex-antiVortex pairs in Red/Blue

Here we see the orientations pertaining to allowed vortices below this vortex explosion temperature. Vortex pair unbinding happens as either force is applied from the current induction, or when the temperature is enough such that their binding energy is already lower than their thermal energy.
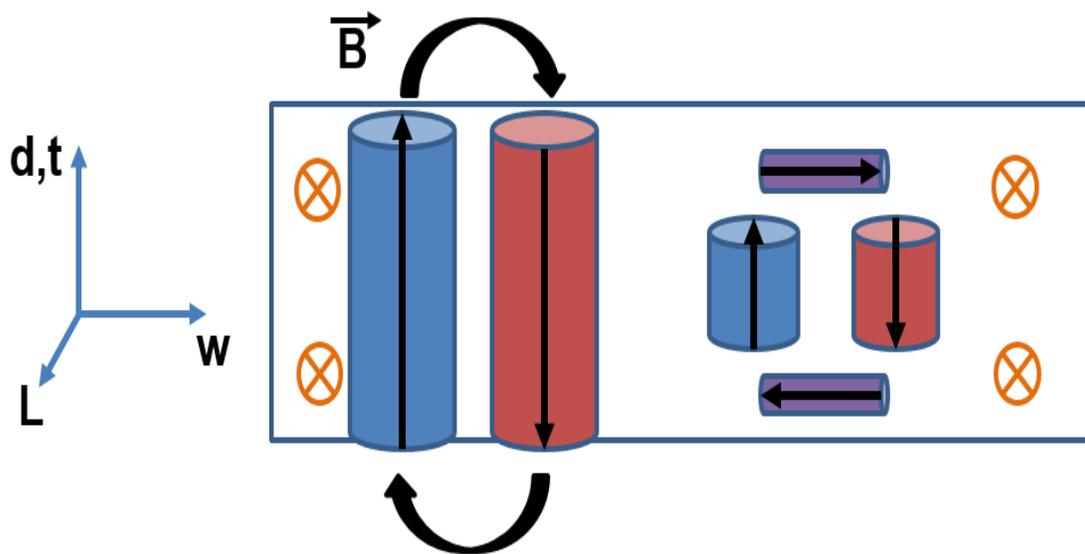
Figure 5.19 Vortex pairs bound outside the condensate (Left) and inside (right)

In Figure 5.18 at the left, the vortex pair completes its binding outside of the superconducting boundary. This is the usual way these pairs are thought to be bound. Pulling them apart stretches the linking B field until they are far enough apart or have enough energy to fully separate them, overcoming the binding energy. On the right, we have a similar pair, but since transverse vortices are allowed in this case, the V-aV pairs are connected inside the condensate. As these are pulled apart, the transverse cores must get longer to facilitate the movement.

However, unlike flux outside the system in air, elongating these cores requires more energy from the system. They will remain attracted no matter how far we pull them, resulting in an infinite binding energy. Because of this, vortex pairs above the T_v will be significantly less likely to unbind. As they are stuck together, they will not flow and will not induce a back *emf* to generate resistance. The more pairs generated in this manner will reduce the net resistance of the system.

5.4 SUMMATION

There remain many open questions about this fascinating system and there may be other possible origins of the superconductivity besides the suggested doping effect, through charge transfer from the Bi_2Te_3 into FeTe. One proposed cause is that some physical torsion applied to the surface of a topological insulator, has enough of an effect on the surface band structure to allow for superconductivity [35]. However, the information obtained in this work provides connections between some key superconducting and normal-state parameters, and it is hoped that this will provide a foundation for future research into this class of systems.

74

Our measurements thus provide evidence for, taking the superconducting thickness from the $B_{c2}(T)$ measurement of He et al. as well as from our I_{VPB} measurement of this work, the second confirmation of the Likharev vortex explosion phenomenon, having been observed before only once in MoGe films [27]. This is the first evidence of Vortex explosion in an insulator-chalcogenide interface superconductor below the Berezinski-Kosterlitz-Thouless transition.

The rather unique sets of experimental curves can be explained through the interplay between current driven unbinding of vortex-antivortex pairs and the Likharev vortex explosion effect. In this work we have provided a second demonstration of this effect and used it as a tool to provide an independent confirmation of the superconducting interface layer thickness, which was previously estimated from $B_{c2}(T)$ measurements. This is novel as the virtual layer of the superconducting state cannot be measured with classical techniques, such as a profilometer or electron microscope.

We also demonstrated here the concept of the vortex-pair-breaking current. Among other things, this also provides yet another tool for estimating the thickness of the superconducting interface layer. More interesting is the extreme current densities that materials with this interface property seem to allow, further pushing the boundary of power transmission with superconductors. With the recent interest in interfacial superconducting systems, these are new interesting effects realizable in such systems and they serve as useful investigative tools for improving our understanding of these systems.

REFERENCE

[1]   Kunchur, M. N., Dean, C. L., Moghadam, N. Shayesteh, Knight, J. M., He, Q. L., Liu, H., Wang, J., Lortz, R., Sou, I. K. & Gurevich, A. (2015). Current-induced depairing in the BTFT interfacial superconductor. *Phys. Rev. B, 92*, 094502.

[2]   Abrikosov, AA (2004). Nobel lecture: Type-ii superconductors and the vortex lattice. *Reviews of modern physics, 76(3)*:975

[3]   Bardeen, J., Cooper, L., & Schrieffer, R. (1957) Theory of superconductivity. *Physical Review, 108*(5):1175,

[4]   Tinkham, M. (2015). Introduction to superconductivity. Mineola, N.Y: Dover Publications.

[5]   Bednorz, J.G. & Muller K. A. (1986). Possible hight c superconductivity in the ba-la-cu-o system. *Zeitschrift fu¨r Physik B Condensed Matter*, 64(2):189–193

[6]   Cecil, T.W. & Weikle, R.M. & Kerr, A. (2007). Investigation of nbtin thin films and aln tunnel barriers with ellipsometry for superconducting device applications. *Applied Superconductivity, IEEE Transactions on, 17(2)*:3525–3528

[7]   Cooper, L.N. (1956) Bound electron pairs in a degenerate fermi gas. *Physical Review, 104(4)*:1189

[8]   Gor'kov, L.P. (1959). Microscopic derivation of the ginzburg-landau equations in the theory of superconductivity. *Sov. Phys. JETP, 9(6):*1364–1367

[9]   Gurevich, A. & Vinokur, V.M. (2008). Size effects in the nonlinear resistance and flux creep in a virtual berezinskii-kosterlitz-thouless state of superconducting films. *Physical review letters, 100(22):*227007

[10]   Kunchur, M.N. (1995) Novel transport behavior found in the dissipative regime of superconductors. *Modern Physics Letters B, 9(07):*399–426

[11]   Kunchur, M.N. (2004). Current-induced pair breaking in magnesium diboride. *Journal of Physics: Condensed Matter, 16(39):*R1183

[12]   Kunchur, M.N. & Dean, C.L. (2015). Current-induced depairing in BiTe/FeTe interfacial superconductor. *Physical Review B, 92(9):*494-502

[13]   Kunchur, M.N. & Liang, M. & Gurevich, A. (2013). The vortex explosion transition. In *Solid State Physics: Proceedings Of The 57th Dae Solid State Physics Symposium 2012, volume 1512*, 19–21

[14]   Landau, L.D. & Ginzburg, V.L. (1950) On the theory of superconductivity. *Zh. Eksp. Teor. Fiz., 20:*1064

[15]   London, F. & London, H. (1935) The electromagnetic equations of the supraconductor. *Proceedings of the Royal Society of London A: Mathematical, Physical and Engineering Sciences, 149(866):*71–88

[16]   Seeber, B (1998) *Handbook of applied superconductivity, volume 2*. CRC press

[17]   Shiino, T. & Shiba, S. & Sakai, N. (2010) Improvement of the critical temperature of superconducting nbtin and nbn thin films using the aln buffer layer. *Superconductor Science and Technology, 23(4):*045004

[18]   Werthamer, N.F. & Helfand, E.F & Hohenberg, P.C. (1966) Temperature and purity dependence of the superconducting critical field, electron spin and spin-orbit effects. *Physical Review, 147(1)*:295

[19]   Zhang, L. & Peng, W. & You, L.X. & Wang, Z. (2015) Superconducting properties and chemical composition of nbtin thin films with different thickness. *Applied Physics Letters, 107(12)*:122603

[20]   Hwang, H. Y. et al. (2012). Emergent phenomena at oxide interfaces. *Natural Materials 11*: 103–113

[21]   Balestrino, G. et al. (2002). Very large purely intralayer critical current density in ultrathin cuprate artificial structures. *Phys. Rev. Lett. 89*, 156-402

[22]   Reyren, N. et al. (2007). Superconducting interfaces between insulating oxides. *Science 317*, 1196–1199

[23]   He, Q.L. et al, (2014). Two-dimensional superconductivity at the interface of a Bi2Te3/FeTe heterostructure. *Nature Communications volume 5,* Article number: 4247

[24]   Stephen, M. J. (1965). Transport Equations for Superconductors. *Phys. Rev. 139*, A197

[25]   Meissner & Ochsenfeld (1933). A new effect on the occurrence of superconductivity. *Naturwissenschaften 21 (44)*: 787–788

[26]   Resnick, D.J.; Garland, J.C.; Boyd, J.T.; Shoemaker, S.; Newrock, R.S. (1981) Kosterlitz Thouless Transition in Proximity Coupled Superconducting Arrays *Phys. Rev. Lett., 47 (21):* 1542

[27]   Blatter, G. & Feigel'man, M. V. & Geshkenbein, V. B. & Larkin, A. I. & Vinokur, V. M. (1994). Vortices in high-temperature superconductors. *Rev. Mod. Phys. 66,* 1125 October

[28]   Kadin, M. & Epstein, K. & Goldman, A. M. (1983). Renormalization and the Kosterlitz-Thouless transition in a two-dimensional superconductor. *Phys. Rev. B 27*: 66-91

[29]   Dean,C.L & Kunchur, M.N. & He, Q.L. (2016). Current Driven Vortex-AntiVortex Pair Breaking and Explosion in Interfacial Superconductors. *Physica C 527* 46–49

[30]   Ginzburg, V.L. and Landau, L.D. (1950). On superconductivity and Superfluidity. *Journal of Theoretical and Experimental Physics 20, 1064*

[31]   Abrikosov , AA (1957). The magnetic properties of superconducting alloys. *Journal of Physics and Chemistry of Solids, 2(3)*, 199–208

[32]   Knight & Kunchur (2008). Flux flow in a two-band superconductor with delocalized electric fields. *Phys. Rev. B 77*, 024516

[33]   Kunchur, Saracila, Arcos, Cui, Pogrebnyakov, Orgiani, X. X. Xi, Adams & Young (2006). Anomalous flux dynamics in magnesium diboride films. *Physica C 437*: 171

[34]   Likharev, K.K. (1979). Superconducting weak links. *Reviews of Modern Physics 51*: 101-115

[35]   Kunchur, M. N., Dean, C., Liang, M., Moghaddam, N. S., Guarino, A., Nigro, A., Leo, A. (2013). Depairing current density of Nd2−xCexCuO4−δ superconducting films. *Physica C: Superconductivity, 495*, 66-68.

[36] Dean, C. L., Kunchur, M. N., Shahesteh-Mogaddam, N., Varner, S. D., Knight, J. M., Ivlev, B. I., . . . Sou, I. K. (2017). Superconductivity and oscillatory magnetoresistance at a topological-insulator/chalcogenide interface. doi:10.1063/1.4980179

[37] M. Z. Hasan and C. L. Kane (2010). *Colloquium*: Topological insulators *Rev. Mod. Phys. 82*, 3045

[38] E. J. Nicol and J. P. Carbotte (2005). Theory of the critical current in two-band superconductors with application to MgB_2. *Phys. Rev. B 72*, 014520

[39] Milind N. Kunchur, David K. Christen, Charles E. Klabunde, and Julia M. Phillips (1994). Pair-breaking effect of high current densities on the superconducting transition in YBaCuO. *Phys. Rev. Lett. 72*, 752

[40] He, M. Q., Shen, J. Y., Petrović, A. P., He, Q. L., Liu, H. C., Zheng, Y., . . . Lortz, R. (2016). Pseudogap and proximity effect in the Bi2Te3/Fe1 yTe interfacial superconductor. *Scientific Reports, 6*(1). doi:10.1038/srep32508

[41] Liang, M., Kunchur, M. N., Fruchter, L., & Li, Z. (2013). Depairing current density of infinite-layer Sr1−xLaxCuO2 superconducting films. *Physica C: Superconductivity, 492*, 178-180. doi:10.1016/j.physc.2013.06.015

[42] Kosterlitz, J. M., & Thouless, D. J. (1973). Ordering, metastability and phase transitions in two-dimensional systems. *Journal of Physics C: Solid State Physics, 6*(7), 1181-1203. doi:10.1088/0022-3719/6/7/010

[43] Kosterlitz, J. M. (1974). The critical properties of the two-dimensional xy model. *Journal of Physics C: Solid State Physics, 7*(6), 1046-1060. doi:10.1088/0022-3719/7/6/005

80